Ocean State Estimation from Hydrography and Velocity Observations During EIFEX with a Regional Biogeochemical Ocean Circulation Model

Martin Losch[a,*], Volker Strass[a], Boris Cisewski[b], Christine Klaas[a], Richard G. J. Bellerby[c,d]

[a] *Alfred-Wegener-Institut, Helmholtz-Zentrum für Polar- und Meeresforschung, Postfach 120161, 27515 Bremerhaven, Germany*
[b] *Johann Heinrich von Thünen Institute, Institute of Sea Fisheries, Palmaille 9, 22767 Hamburg, Germany*
[c] *Norwegian Institute for Water Research, Bergen, Thormøhlensgate 53 D, N-5006 Bergen, Norway*
[d] *Uni Research, University of Bergen. Allegaten 55, N-5007 Bergen, Norway*

Abstract

In the European Iron Fertilization EXperiment (EIFEX), the iron hypothesis was tested by an open ocean perturbation experiment. The success of EIFEX owes to the applied experimental strategy; namely to use the closed core of a mesoscale eddy for the iron injection. This strategy not only allowed tracking the phytoplankton bloom within the fertilized patch of mixed-layer water, but also allowed the export of biologically fixed carbon to the deep ocean to be quantified. In this present study, least-squares techniques are used to fit a regional numerical ocean circulation model with four open boundaries to temperature, salinity, and velocity observations collected during EIFEX. By adjusting the open boundary values of temperature, salinity and velocity, an optimized model is obtained that clearly improves the simulated eddy and its mixed layer compared to a first guess representation of the cyclonic eddy. A biogeochemical model, coupled to the optimized circulation model, simulates the evolution of variables such as chlorophyll *a* and particular organic carbon in close agreement with the observations. The estimated carbon export, however, is lower than the estimates obtained from observations without numerical modeling support. Tuning the sinking parameterization in the model increases the carbon export at the cost of unrealistically high sinking velocities. Repeating the model experiment without adding iron allows more insight into the effects of the iron fertilization. In the model this effect is about 40% lower than in previous estimates in the context of EIFEX. The likely causes for these discrepancies are potentially too high remineraliza-

---

[*] Corresponding author, email: Martin.Losch@awi.de, ph.: ++49 (471) 4831-1872, fax: ++49 (471) 4831-1797

tion, inaccurate representation of the bloom-termination in the model, and ambiguity in budget computations and averaging. The discrepancies are discussed and improvements are suggested for the parameterization used in the biogeochemical model components.

Keywords: REGIONAL MATHEMATICAL OCEAN MODEL, POLAR FRONT, BIOGEOCHEMISTRY, DATA ASSIMILATION, IRON FERTILIZATION, EXPORT FLUXES, EIFEX, MITGCM, RECOM

---

1. Introduction

Modeling biogeochemical processes and ecosystems in the ocean poses a number of challenges. Firstly, the biogeochemical processes themselves are complex and require many parameterizations. Typically, the modeler's individual interests lead to a particular set of parameterizations and differential equations and, subsequently, to very different numerical models. Secondly, biogeochemical processes are largely controlled by their physical environment. Physical circulation and mixing transport nutrients into the euphotic zone where the available light for phytoplankton growth is determined by the depth of the mixed layer and the rate of vertical exchange. Only if both nutrients and light are available, will phytoplankton grow and provide food for grazers. A numerical model of ocean ecosystems must therefore accurately simulate all of these processes. In this paper, we address modeling biogeochemical processes in the open ocean with a particular focus on finding an appropriate circulation that controls the biogeochemical processes.

Numerical ocean models require testing and tuning against *in-situ* observations. Only after a numerical model passes such a test it can be used with confidence for simulating unobserved properties. Systematic tuning to improve the fit between a model and observations is termed data assimilation or state estimation and a vast amount of literature exists on this subject (e.g, Bennett, 2002, Wunsch, 2006). Most data assimilation techniques are based on a least-squares-fit between model results and observations.

In oceanography data and, in particular, sub-surface data are sparse and the prediction skill of ocean models tends to be poor over longer time scales. In this paper, we present a state estimation experiment on a short time scale, in which we exploit the availability of a high-resolution regional data set. Hydrographic, chemical and biological tracers, and velocity data from the European Iron Fertilization EXperiment (EIFEX, Smetacek et al., 2012) are used to constrain a high-resolution coupled ecosystem-ocean circulation model of the experimental site in the Atlantic sector of the Antarctic Polar Frontal Zone (PFZ).

State estimation with variational techniques, where a model is fit to all available observational data simultaneously, is the obvious choice if a dynamically consistent analysis of observations (or dynamically consistent interpolation between observations) is required (Wunsch, 2006). With variational methods the dynamics of the numerical model are not altered, but initial and boundary conditions, collected in the control vector, are adjusted in order to fit the model to the observations. We use a regional model in which the open boundaries are part of the control vector, because the observations are concentrated in a small box of approximately 200 by 150 km. Other studies have demonstrated the feasibility of this approach (e.g., Seiler, 1993, Schröter et al., 1993, Zhang and Marotzke, 1998, Vogeler and Schröter, 1999, Ayoub, 2006, Lea et al., 2006, Gebbie et al., 2006, Dwivedi et al., 2011). Here we can afford a horizontal resolution of approximately 3.6 km, which is higher than used in previous studies known to the authors, because the domain is small.

With a coupled biogeochemical ocean circulation model one would, ultimately, like to estimate the state of the ecosystem simultaneously with the state of the ocean physics. Undertaking this task is beyond the scope of our work as it involves strong non-linearities (attributed to the ecosystem model) that cannot be treated consistently with variational techniques. Instead a two-step approach is taken. First, the ocean model is fit to observations of hydrography, velocity and surface forcing with the help of variational state estimation to obtain the "optimal" physical trajectory. The numerical model we use is the Massachusetts Institute of Technology general circulation model (Marshall et al., 1997, MITgcm Group, 2012) together with the ECCO infra-structure for state estimation (see, e.g., Stammer et al., 2002, 2003, Gebbie et al., 2006). This optimal trajectory is used to "drive" the ecosystem model. For now we only use a "tuning by hand" approach to optimize the ecosystem model, but more sophisticated parameter methods are available (e.g., particle filters, Kivman, 2003). Second, the ecosystem is coupled to the full 3D physical model to obtain estimates of primary production and vertical transport of carbon and other tracers. This procedure ensures that the model dynamics of both physical and ecosystem model are preserved during the time of the integration.

After simulating the trajectory of the coupled biogeochemistry-ocean system following iron fertilization as accurately as possible, we can repeat the experiment without iron fertilization. Comparing simulations with and without fertilization gives us an advantage over field experiments, which cannot be repeated in the same way, and leads to more insights into export dynamics.

In the following Section 2, we provide a short overview of the iron fertilization experiment EIFEX and the available observations. In Section 3 the circulation model and the optimization technique are described. Section 4 presents results of the optimization of the circulation model with the help of *in-situ* observations of temperature, salinity, and velocity. Section 5 describes the Regulated Ecosystem Model (REcoM, Schartau et al., 2007, Hohn, 2009) and discusses results that can be obtained with the coupled system. Conclusions are drawn in Section 6.

2. A short description of EIFEX

EIFEX (European Iron Fertilization Experiment) tested the hypothesis that iron limits primary production and the biological pump of carbon in the Southern Ocean (Smetacek et al., 2012). A mesoscale cyclonic eddy was found as a suitable site for the open ocean experiment with the help of satellite altimetry data (`http://eddy.colorado.edu/ccar/data_viewer/index`) and an *in-situ* survey (Strass et al., 2005). The eddy was embedded in a meander of the Antarctic Polar Front and extended over an area of 60 km by 100 km, with the center near 49°24' S and 02°15' E in the South Atlantic. Inside the eddy, a 167 km^2 patch was fertilized with dissolved iron on February 12–13. Subsequently the biogeochemical and ecosystem response was monitored. A second fertilization of the expanded patch (740 km^2) took place on February 26–27, 2004. During the course of the experiment, hydrographic and dynamic variables as well as biological and chemical properties were measured at stations inside and outside the fertilized patch along the ship track. The water column was monitored down to 500 m depth. For the physical analysis, we use *in-situ* measurements of temperature and salinity from a conductivity-temperature-depth (CTD) sonde, data from a ship-mounted thermosalinograph that continuously measured surface temperature and salinity and finally current velocities from both a buoy-tethered and a ship-mounted Acoustic Doppler Current Profiler (ADCP). Measurements covered a region extending from approximately 1° E to 4° E and 48° S to 51° S and spanned the period from February 08 (day 1) to March 16 (day 38), 2004.

The cruise track and the CTD station positions for this period are shown in Figure 1. After the first fertilization on February 12–13 an ADCP survey together with CTD measurements and water sampling were carried out on a regular grid (GRID 5). GRID 5 covered an area of approximately 150 by 200 km. The remaining cruise track more or less followed the fertilized patch, which was fertilized a second time on February 26–27, and hydrographic and biogeochemical parameters were measured with a high temporal resolution. Figure 2 (left column) shows the surface temperature and salinity distributions estimated from GRID 5 data. Figure 3 portrays the stream function estimated from the GRID 5 ADCP survey (see also Cisewski et al., 2008).

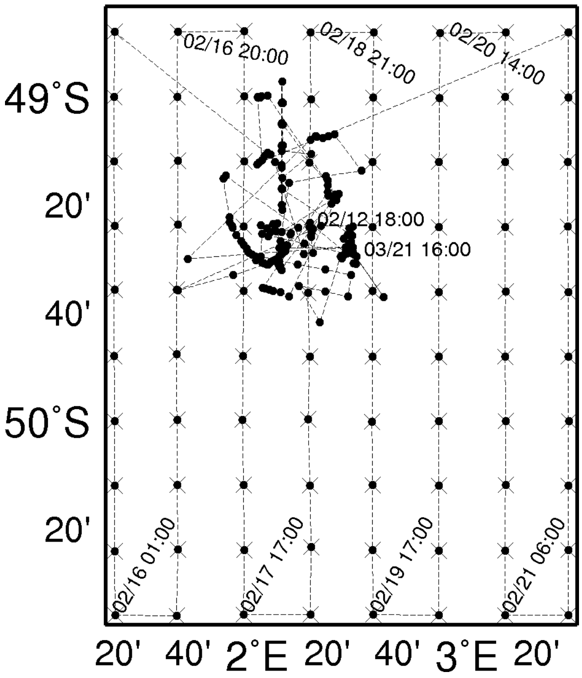

Figure 1: Cruise track (dashed line) and positions of the CTD-stations (dots). Station positions of GRID 5 that were covered in the first 10 days after the first fertilization are marked by crosses. Date (in 2004) and time of selected stations are indicated by numbering.

3. Circulation Model and State Estimation

We use the Massachusetts Institute of Technology general circulation model (MITgcm). This general purpose, finite-volume algorithm is configured so that in the present context it solves the Boussinesq and hydrostatic form of the Navier-Stokes equations for an incompressible fluid on a three-dimensional longitude λ, latitude φ, depth H grid. The general algorithm is described in Marshall et al. (1997), for online documentation and access to the model code, see `http://mitgcm.org` (MITgcm Group, 2012).

In order to combine model and data for the best possible estimate, we use the adjoint method for solving a constrained least-squares problem as described in Thacker and Long (1988). In this assimilation technique, a global (in space and time) objective function of squared data-model misfits is minimized by an iterative process which repeatedly integrates the forward circulation model followed by the adjoint circulation model. The adjoint model integrations yield the gradient of the objective function with respect to the independent control variables. A minimization algorithm (here the BFGS algorithm adapted from Gilbert and Lemaréchal, 1989) uses this information to determine a new set of control variables that lead to a smaller objective function value. The MITgcm has been adapted to allow the use of the Tangent linear and Adjoint Model Compiler (TAMC), and its successor TAF (Transformation of Algorithms in Fortran, Giering and Kaminski, 1998), to conveniently generate efficient and exact code for the adjoint model (Heimbach et al., 2002, 2005). The model code together with the adjoint method was used previously in the ECCO context (Stammer et al., 2002, 2003, Stammer, 2005, Losch and Heimbach, 2007, Gebbie et al., 2006) and by, for example, Ferreira et al. (2005).

The present application of the MITgcm and its adjoint requires a domain with four open boundaries. We use a configuration that is similar to that of Gebbie et al. (2006), but with a much smaller domain covering a rectangle of approximately 150 by 194 km with the south-east corner at 1°21' E and 50°33' S and a high horizontal resolution (approximately 3.6 km). Vertical layer thicknesses are 10 m between the surface and 150 m depth and increase monotonically to 25 m at 500 m depth. The resulting grid consists of 42×54 horizontal grid cells and 30 vertical layers. The bottom of the domain is flat and impermeable for physical processes, but biogeochemical tracers may sink "through" the bottom out of the domain.

Surface boundary conditions are prescribed as horizontal wind stress and heat and freshwater fluxes estimated from meteorological observations during the EIFEX cruise (10 m wind velocity, 2 m air temperature, specific humidity, global radiation; POLDAT, König-Langlo and Marx, 1997) and bulk formulae (Large and Pond, 1981, 1982). Observations of precipitation are only available for the first half of the experiment due to instrument failure during the latter half; for the second half precipitation is assumed to be constant and equal to the mean of the observations of the first half of the experiment. Downward long wavelength radiation is estimated from observations of cloud cover and air temperature according to König-Langlo and Augstein (1994). At the open boundaries temperature, salinity, and horizontal velocities are prescribed independently, so that in the general case the fields at the boundaries may not be in geostrophic balance. Prescribed values are estimated from interpolated data collected during GRID 5 (Figure 1) on the first 10 days of the experiment.

The circulation of the numerical model is determined by the initial and boundary conditions. Therefore, the control vector of the state estimation problem consists of initial conditions for temperature and salinity, daily corrections to the surface boundary fluxes of heat, freshwater, and momentum, and, most important, of daily corrections to the boundary values for temperature, salinity, and horizontal velocity. Note that in contrast to sequential methods, all control variables are adjusted simultaneously. In all cases, except for the initial conditions, only the daily averaged corrections are included in the control vector in order to reduce the number of controls. These corrections are linearly interpolated in time. Still, the length of the control vector is approximately 1.4 million for a 39 day integration.

The control vector is adjusted to minimize the following objective function:

$$\begin{aligned}\mathcal{J} = \frac{1}{2}\sum_{ij}\Big\{ & (\theta_i - \theta_i^*)^T W_{ij}^{(\theta)} \left(\theta_j - \theta_j^*\right) \\ & + (S_i - S_i^*)^T W_{ij}^{(S)} \left(S_j - S_j^*\right) \\ & + (u_i - u_i^*)^T W_{ij}^{(u)} \left(u_j - u_j^*\right) \\ & + (v_i - v_i^*)^T W_{ij}^{(v)} \left(v_j - v_j^*\right)\Big\} \\ + & \quad \text{other terms.}\end{aligned} \tag{1}$$

The starred symbols denote observations of potential temperature θ, salinity S, and horizontal velocities (u, v) mapped to the model grid at a certain point in (model) space and time. The data are assumed to be representative for a given day and the corresponding model variables in function (1) are daily averages. The weights W are the inverses of the data error covariances. There is not enough information about the data correlations—even though one could construct vertical error covariances as in Losch and Schröter (2004). Therefore, we assume horizontally homogeneous and uncorrelated errors and the weights become $W_{ij} = \delta_{ij}\sigma_i^{-2}$, where δ_{ij} is the Kronecker symbol and σ_i the uncorrelated error. These errors are listed in Table 1. For temperature and salinity the errors are estimated per layer from the horizontal standard deviation of the observations within the eddy and a minimum error of 0.2 °C for temperature and 0.02 for salinity is imposed. The velocity error is assumed constant at $10\,\mathrm{cm\,s^{-1}}$.

The "other terms" in function (1) are the sums of the squared deviations of the daily means from their respective first guesses of surface stresses (τ_x, τ_y), surface fluxes of heat Q and fresh water $(E - P)$ (evaporation minus precipitation) and the open boundary values (OB). In vector-matrix notation

Table 1: Prior data error estimates used in the objective function (1).

layer	depth	$\sigma^{(\theta)}$ (°C)	$\sigma^{(S)}$	$\sigma^{(u,v)}$ (cm s^{-1})
1	5.00 m	0.2834	0.0396	10.0
2	15.00 m	0.2000	0.0200	10.0
3	25.00 m	0.2000	0.0200	10.0
4	35.00 m	0.2000	0.0200	10.0
5	45.00 m	0.2000	0.0200	10.0
6	55.00 m	0.2000	0.0200	10.0
7	65.00 m	0.2000	0.0200	10.0
8	75.00 m	0.2000	0.0200	10.0
9	85.00 m	0.2048	0.0200	10.0
10	95.00 m	0.2000	0.0200	10.0
11	105.00 m	0.2622	0.0200	10.0
12	115.00 m	0.4424	0.0200	10.0
13	125.00 m	0.4786	0.0200	10.0
14	135.00 m	0.4881	0.0214	10.0
15	145.00 m	0.5862	0.0268	10.0
16	156.00 m	0.6418	0.0340	10.0
17	170.25 m	0.6012	0.0370	10.0
18	189.25 m	0.4528	0.0362	10.0
19	212.50 m	0.2000	0.0258	10.0
20	237.50 m	0.2000	0.0222	10.0
21	262.50 m	0.2000	0.0320	10.0
22	287.50 m	0.2084	0.0478	10.0
23	312.50 m	0.3688	0.0716	10.0
24	337.50 m	0.3330	0.0728	10.0
25	362.50 m	0.3320	0.0702	10.0
26	387.50 m	0.2566	0.0568	10.0
27	412.50 m	0.2252	0.0388	10.0
28	437.50 m	0.2234	0.0372	10.0
29	462.50 m	0.2000	0.0278	10.0
30	487.50 m	0.2000	0.0264	10.0

these are:

$$
\begin{aligned}
\text{other terms} \quad = \quad & \delta\tau_x^T\,\mathbf{W}_{\tau_x}\,\delta\tau_x \\
& + \delta\tau_y^T\,\mathbf{W}_{\tau_y}\,\delta\tau_y \\
& + \delta\mathbf{Q}^T\,\mathbf{W}_Q\,\delta\mathbf{Q} \\
& + \delta(\mathbf{E}-\mathbf{P})^T\,\mathbf{W}_{E-P}\,\delta(\mathbf{E}-\mathbf{P}) \\
& + \delta\theta_{OB}^T\,\mathbf{W}_\theta^{OB}\,\delta\theta_{OB} \\
& + \delta\mathbf{S}_{OB}^T\,\mathbf{W}_S^{OB}\,\delta\mathbf{S}_{OB} \\
& + \delta\mathbf{u}_{OB}^T\,\mathbf{W}_u^{OB}\,\delta\mathbf{u}_{OB} \\
& + \delta\mathbf{v}_{OB}^T\,\mathbf{W}_v^{OB}\,\delta\mathbf{v}_{OB}.
\end{aligned}
\tag{2}
$$

These terms introduce prior knowledge about the solution and ensure that the solution does not differ from the first guess by an unrealistic amount (specified by the weights). As before the prior errors are assumed to be uncorrelated and homogeneous in space and time. For the surface fluxes, they are $0.02\,\mathrm{N\,m^{-2}}$ for wind stress, $2.0\,\mathrm{W\,m^{-2}}$ for net heat flux, and $2\times10^{-9}\,\mathrm{m\,s^{-1}}$ for fresh water flux. The prior errors for the open boundary values are the same as those listed in Table 1, except that the errors for temperature and salinity are scaled by 0.1.

4. Results

4.1. First guess

Data collected during the first 10 days of the experiment (GRID 5) are used to estimate a first guess of initial conditions and stationary open boundary values for temperature, salinity, and horizontal velocity by bilinear interpolation (where possible) or “nearest” extrapolation. Time-varying boundary conditions, while desirable, cannot be derived from the available observations, but in the optimized solution (Section 4.2), the boundary conditions become time dependent because of the correction inferred from the model-data misfit. The initial guesses of surface boundary conditions are estimated every hour from ship-based meteorological observations, and they are assumed to be uniform in space. The control variables are the time-varying deviations from these first guesses.

With these initial and boundary conditions, the eddy in the model domain quickly moves to the north where it “leans” on the open boundary (Figure 2, middle column). Also, its diameter is notably smaller than in the estimate from observations. Warm and fresh water is advected into the domain from the west and the north-eastern corner of the domain, and a tongue

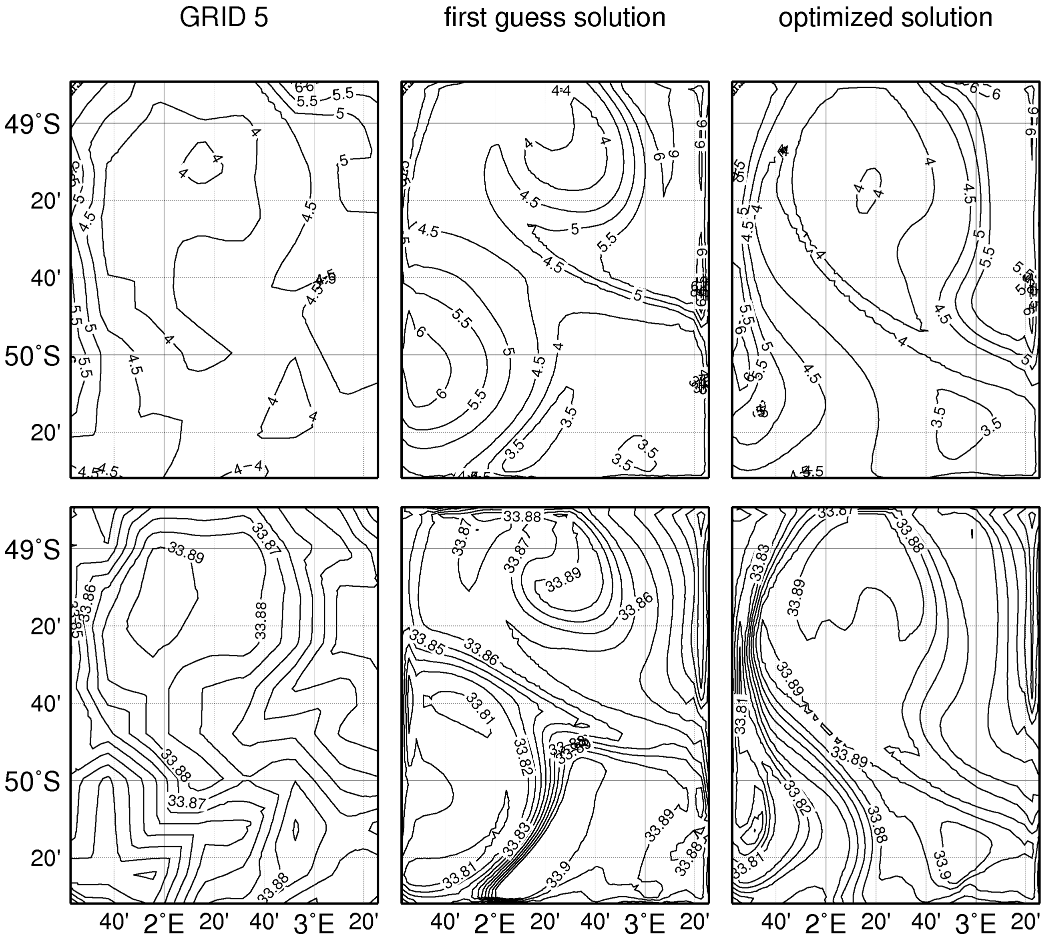

Figure 2: Comparison of surface temperature (top) and salinity (bottom) fields from observations (GRID 5), first guess model solution, and optimized model solution (averages over the first 10 days). Contour interval is 0.5 °C for temperature and 0.01 for salinity.

of warm and fresh water intrudes into the center of the eddy (Figure 2, middle column).

The observed deepening, warming, and freshening of the mixed layer is shown in the uppermost panel of Figure 4. In the first guess solution, however, the mixed layer is shallower than in the observations (Figure 4, bottom panel). The first guess solution does not reproduce the warming and freshening accurately that is visible in the observations.

4.2. Optimized solution

Here, we present a solution that we obtain after 171 iterations of the minimization algorithm. The reduction of the total cost (value of the objective function) between two iterations has become small at this point of the mini-

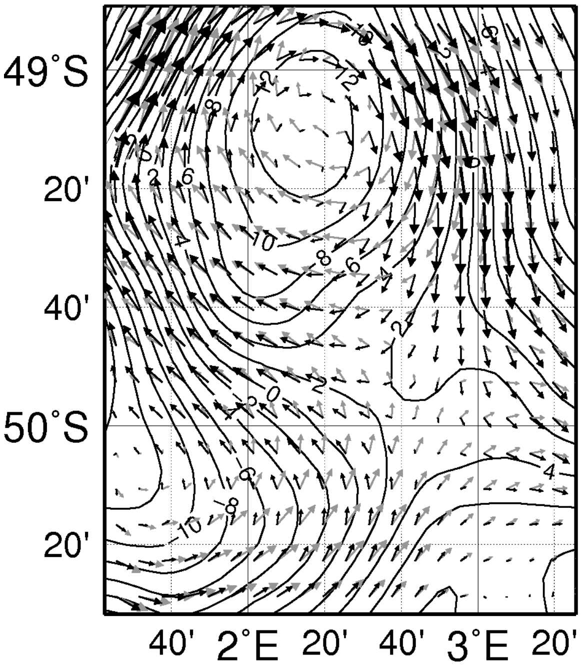

Figure 3: Comparison of current field between 150 m and 200 m depth. Contours are the stream function estimated from observations (GRID 5, see also Cisewski et al., 2008), grey vectors indicate first guess model velocities, and bold black vectors optimized model velocities (averages over the first 10 days and 150 to 200 m depth). Vector size indicates current strength.

mization and we assume that the solution is useful (to be shown *a posteriori*). Figure 5 shows the individual contributions to the objective function, normalized by the initial total cost. The total cost is reduced to less than 18% of the initial value and the last iteration reduced the objective function by 0.01% of the initial value. Note that fitting the model trajectory to the data (as seen in the reduction of the data terms, thick dashed and dash-dotted lines in Figure 5) is mostly achieved at the “cost” of deviating from the first guess of the open boundary conditions. The surface fluxes play a secondary role on the short timescales that are relevant here. Within the contribution of the open boundary conditions to the cost function the largest deviation from the first guess is found in the horizontal velocities (not shown). This partition of the overall cost is anticipated by the choice of the prior weights because the uncertainty of the open boundary values for velocities is large due to the non-synopticity and extrapolation of the data while the surface fluxes are based on *in-situ* observations and only small errors are associated with them. The root-mean-square (rms) of the difference between observed and simulated daily mean u-(v-)component of the velocity is reduced from

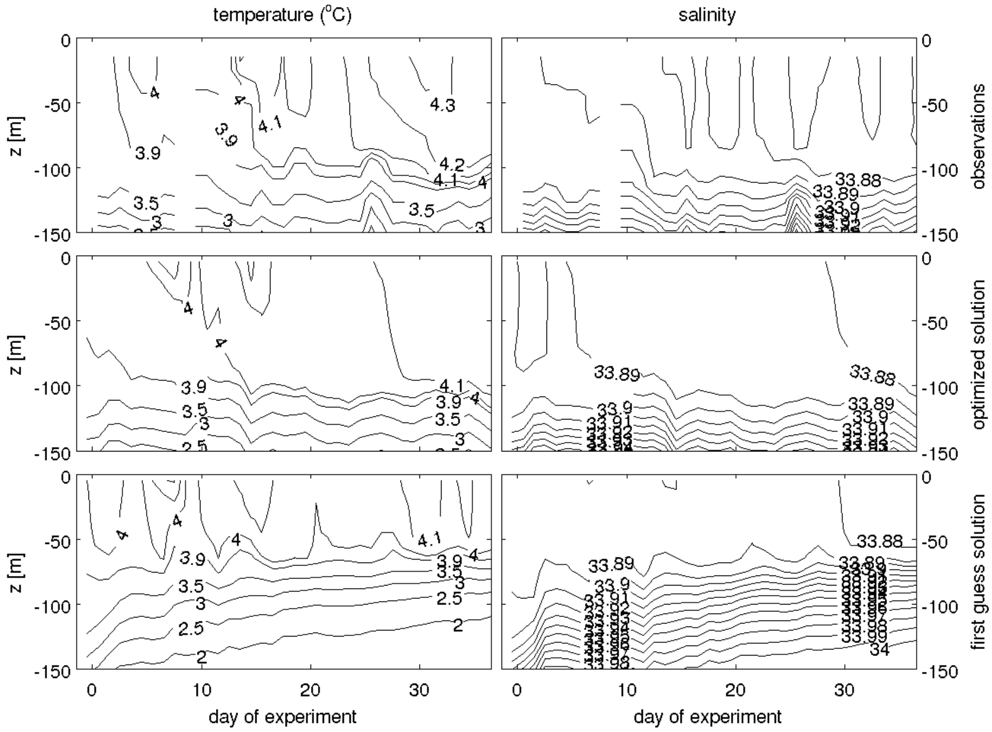

Figure 4: Temperature and salinity evolution near the surface averaged over the eddy. Top: observations, middle: optimized solution, bottom: first guess solution.

25 (23) cm/s to 9.0 (9.6) cm/s. This is considered a success, as these values are smaller than the prior error of 10 cm/s, especially since the per-layer-rms of the model-data misfits for temperature and salinity are also smaller or the same size as their prior errors. The same is true for the regularization terms in Eq. (2).

The resulting flow field is significantly improved over the first guess solution (Figure 3). The eddy now stays near the observed position and warm and fresh water does not penetrate into the domain from the west. There is still an inflow of warm and fresh water from the north because there are not enough observations to constrain the model trajectory in this area. The inflowing warm and fresh water, however, does not reach the core of the eddy but is deflected and leaves the domain again at the eastern boundary (Figure 2). After the first 10 days of the experiment observations are restricted to the core of the eddy. Still the eddy in the optimized solution stays close to the observed position throughout the entire integration as will be shown with independent observations in Section 5.3.

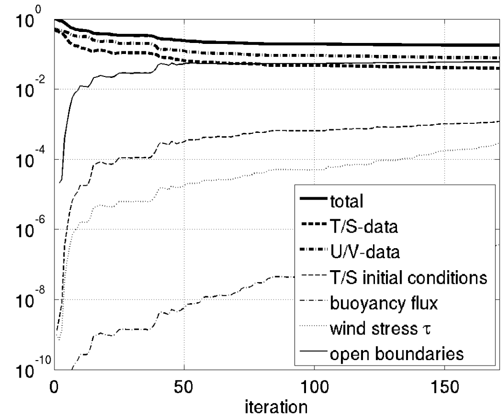

Figure 5: Objective function contributions as a function of iteration number. All values are scaled by the initial total objective function value of 2.374×10^{6}.

The simulated flow field is generally less variable than the observed one: the rms-values of the daily mean of the observed velocity components u and v are 20 and 26 cm/s; the rms-values of the corresponding model variables are 18 and 24 cm/s. One consequence is that the model underestimates the vertical velocity shear: The mean shear of the daily averaged ADCP-observations (estimated as the mean of $\partial\sqrt{u^2+v^2}/\partial z$ over all daily averages) is of order 2.5×10^{-3}/s; for the corresponding model variables this value is 0.8×10^{-3}/s.

Vertical mixing and light availability are important factors controlling phytoplankton blooms. Therefore, we consider the improved description of the mixed layer depth within the eddy (Figure 4) as the main success of the optimization. The optimized model reproduces most of the the observed fluctuations in the temperature and salinity profiles. Similarly, the modeled mixing parameters (actively mixing layer, computed diffusivity coefficients) agree with the observations (Figure 6, see also Cisewski et al., 2008, their Figure 9). For example, Cisewski et al. (2008) compare vertical diffusivities and actively mixed layer depths computed from a Thorpe scale analysis of micro-structure sonde (MSS) profiler data with model estimates of the mixed-layer model KPP (Large et al., 1994); they find average vertical diffusivities in the actively mixed layer of 2.84×10^{-2} m^2 s^{-1} (MSS observations) and 3.39×10^{-2} m^2 s^{-1} (KPP in this model) and time mean boundary layer depths of 66.4 ± 28.8 m (MSS observations) and 69.1 ± 29.5 m (this model). The model solution, however, still underestimates the temporal variability in the mixed layer depth, in particular the warming and freshening of the mixed layer that starts around day 30 of the experiment. Below the mixed layer

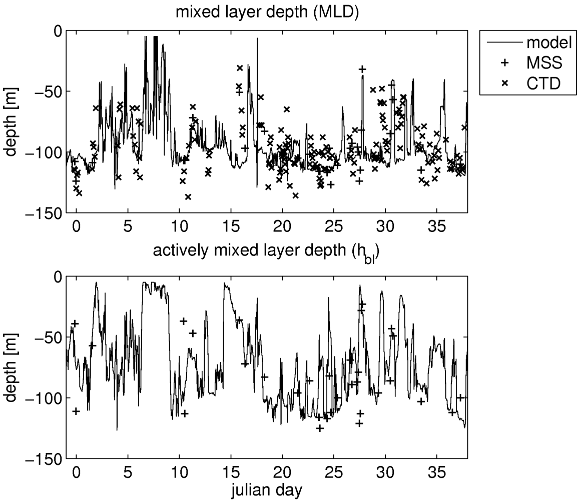

Figure 6: Comparison of mixed layer depth and actively mixing layer depth as estimated by the KPP model embedded in the circulation model, from Thorpe scale analysis of micro-structure sonde (MSS) profile data and from CTD profiles. See text and Cisewski et al. (2008) for more details.

depth the water column is mostly stable and vertical diffusivity remains near the background value of $10^{-5}\ \mathrm{m}^2\,\mathrm{s}^{-1}$.

Physically and biologically inert tracers such as sulfur hexafluoride (SF_6) were not released during EIFEX, but photosynthetic efficiency (Fv/Fm) and later pCO2 and chlorophyll *a* were shown to be, in this case, good indicators for tracking the fertilized patch (Smetacek et al., 2012). Patch dilution rates, however, are more difficult to estimate without appropriate inert tracer observations. In the optimized model we address this issue and estimate the dispersion of the fertilized patch from an idealized tracer release experiment: At the simulated day of the first iron release, an inert tracer is released instead of iron; the mean squared radial distance of a tracer particle from the center of the patch is computed from the first three moments of the surface tracer concentration C (total area M_0, center of mass M_1, and dispersion M_2) as (Stanton et al., 1998, Martin et al., 2001)

$$W^2 = \frac{M_2}{M_0} - \left(\frac{M_1}{M_0}\right)^2. \tag{3}$$

The area integrated moments are defined by $M_k = \int\int C\, r^k\, dx\, dy$, with the distance r from the center of mass (Figure 7). A linear regression gives a mean increase of the patch area (mean squared radial distance) of roughly $9.6\ \mathrm{km}^2\,\mathrm{d}^{-1}$, so that the patch size increased approximately 20 times during the experiment. During this time the total amount of tracer decreased by

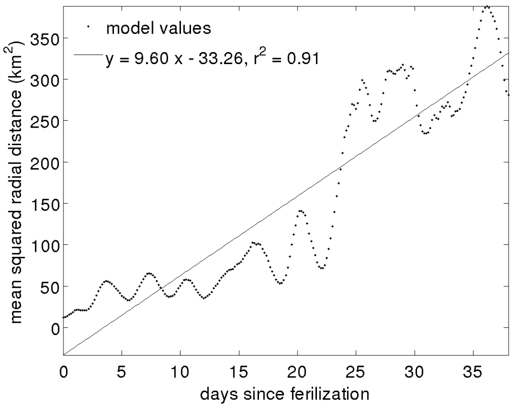

Figure 7: Mean squared radial distance from patch center of an idealized tracer as a function of time estimated from the first moments of the tracer distribution (dots). Also shown is the linear fit (solid line).

7.3% (not shown) indicating very little loss across the domain boundaries. The corresponding estimate of the horizontal mixing (diffusion) coefficient is approximately $9.6\ \mathrm{km}^2/86400\,\mathrm{s}/2 \approx 56\,\mathrm{m}^2\,\mathrm{s}^{-1}$. Hibbert et al. (2009) inferred an upper limit of diffusivity of $87\pm20\,\mathrm{m}^2\,\mathrm{s}^{-1}$ from diffusive heat budgets for isopycnic (horizontal) mixing combined with the observed rate of warming during EIFEX. From the linear regression in Figure 7, the dilution rate is estimated as the rate of change of patch area divided by the mean patch area: $9.6\ \mathrm{km}^2\,\mathrm{d}^{-1}/150\ \mathrm{km}^2 = 0.064\,\mathrm{d}^{-1}$. Smetacek et al. (2012) give a range of dilution rates of 0.06–$0.1\,\mathrm{d}^{-1}$ based on various estimation techniques including ours.

5. Experiments with a Regulated Ecosystem Model

The expedition EIFEX was designed and carried out to assess the impact of an iron fertilization on the ecosystem in a high-nutrient-low-chlorophyll (HNLC) region. Monitoring the effect of fertilizing the surface ocean on the biological pump, that is, the drawdown of atmospheric CO_2 and the subsequent vertical flux of carbon into the deep ocean, was central to EIFEX. Based on the measurements conducted during EIFEX, the vertical carbon flux was estimated indirectly, for example from budgets of dissolved and particulate carbon as well as nutrients in the upper 100 m, from the decrease of *in-situ* concentrations of particle-reactive isotopes. However, while the data coverage during EIFEX is exceptional when compared to the general data coverage in survey studies, many quantities of interest could not be observed directly.

In order to supplement these estimates, and to concurrently improve parameterizations used in models that describe biogeochemical functional relationships, an ecosystem model is coupled to the numerical model of the physical trajectory. This ecosystem model is tuned to reproduce the observed biological quantities with a special focus on chlorophyll concentration, particular organic carbon and nitrogen (POC and PON), and nutrient distribution. Observations of phytoplankton and zooplankton biomass concentrations were also used to tune the model. Then the model provides a full three-dimensional trajectory of both observed and unobserved quantities (e.g., detritus), from which target quantities such as vertical carbon flux, carbon uptake, or total organic matter, and further the iron-fertilization efficiency can be diagnosed. The model estimates are "optimal" in the sense that their deviations from both the estimated physical trajectory and the observed biological quantities are minimized.

5.1. Ecosystem model

In our study we use the Regulated Ecosystem Model (REcoM, Schartau et al., 2007), which is based on an approach of Geider et al. (1998) with extensions by Hohn (2009). In contrast to many other models, carbon and nitrogen fluxes in REcoM are decoupled and do not rely on fixed Redfield ratios (see also Taylor et al., 2013).

For Southern Ocean applications, REcoM has been extended to account for diatom blooms, opal export, and iron explicitly (Hohn, 2009, Taylor et al., 2013). Four additional state variables have been added: silicic acid, iron, and biogenic silica in phytoplankton and detritus. The assimilation of inorganic silicon depends on algal growth rates that are expressed in terms of nitrogen utilized by diatoms. Upper and lower limits are prescribed for the cellular silicon-to-nitrogen (Si:N) ratio. For example, silicate assimilation ceases (is down-regulated) under nitrogen limitation after the cellular Si:N has reached a maximum value. A simple Michaelis-Menten parameterization is used for iron utilization by phytoplankton. Iron uptake is coupled to the modeled photosynthetic rates. The model approach requires a prescribed fixed cellular iron-to-carbon (Fe:C) ratio, thus allowing variations of the cellular iron-to-nitrogen (Fe:N) ratio. Hence, light limitation may inhibit iron uptake and silicic acid utilization depends on nitrogen uptake.

All state variables C of the ecosystem model are advected and mixed according to the physical trajectory; locally they change according to the ecosystem dynamics $S_A(C)$ that are specific to C:

$$\frac{\partial C}{\partial t} + \nabla \left(\mathbf{u} C - \kappa \left[\nabla C - \mathbf{z} \hat{\gamma} \right] \right) = S_A(C), \tag{4}$$

where $\mathbf{u}$ is the three-dimensional velocity, κ the tensor of mixing coefficients and $\mathbf{z}\hat{\gamma}$ the vertical "counter gradient flux" specific to the KPP mixing scheme (Large et al., 1994). The vertical flux of C is the z-component of the second term in Eq. (4):

$$(w - |w_s|)\, C - \kappa_v \left[\frac{\partial C}{\partial z} - \hat{\gamma}\right], \tag{5}$$

where w is the vertical velocity, $|w_s|$ the sinking velocity (only > 0 for negatively buoyant particles), and κ_v the vertical diffusivity. Sinking out of a grid cell is parameterized as a function of local (parameterized) aggregation of nitrogen particles and detritus mass within the grid cell (i.e. above the grid location of the sinking velocity) as:

$$|w_s(\mathbf{x})| = a|z|\ (a_{PD} D_N(\mathbf{x}) + a_{PP} P_N(\mathbf{x})) \tag{6}$$

with a constant parameter $a = 5\,\mathrm{d}^{-1}$ and the coordinate vector $\mathbf{x} = (x, y, z)$; z is the vertical coordinate in meters. The depth dependence of w_s follows, for example, Kriest and Oschlies (2008). Note that the aggregates concentration $a_{PD}D_N + a_{PP}P_N$ is not a separate variable, but it is parameterized by nitrogen in detritus D_N and in phytoplankton P_N (both 3D fields) and the constant aggregation parameters a_{PD} and a_{PP} (see appendix). In our experiments, only detritus, which is assumed to include, for example, fecal pellets, sinks with this velocity. With our choice of parameters, the sinking velocity (6) easily reaches $100\,\mathrm{m\,d}^{-1}$ beneath the mixed layer. Note that expression (6) parameterizes an effective sinking velocity that represents an average over all (unresolved) size classes in the model. Such an effective sinking velocity is necessarily lower than the settling speeds of over $500\,\mathrm{m\,d}^{-1}$ postulated in Smetacek et al. (2012) for large aggregates in the centimeter size range and in the center of the patch (so-called "hot-spot").

Further details of the model and the model equations (right hand sides S_A in Eq. (4)) can be found in the appendix.

5.2. Optimizing REcoM

REcoM contains a suite of tunable parameters. As a first effort, the model is tuned to fit the observations of chlorophyll, POC, PON, and nutrient concentrations by varying individual parameters or combinations of parameters. For a more objective method to fit the model to observations as for the physical state, non-linear state estimation techniques (e.g., Kivman, 2003, Schartau and Oschlies, 2003) are required. Our heuristic tuning exercise suggests that on the short time scale of this experiment, the fit of the model to the observations is most sensitive to the growth parameters (i.e., the maximal growth rate p^{*}_{max} and the slope of the initial PI-curve α), the grazing and mortality rates, and the aggregation rates a_{PP} and a_{PD} in combination with the vertical sinking velocity of detritus (Eq. (6)). See Table A.3 in the appendix for a list of all model parameters and their values.

5.3. 3D-Results with REcoM

Initial conditions and open boundary values for the ecosystem state variables are prescribed as follows: for those quantities, for which we have enough observations to estimate a quasi-synoptic field, this field (often only a vertical profile) is used as both initial condition and constant (in time) Dirichlet boundary conditions: dissolved inorganic nitrogen (DIN), inorganic carbon (DIC), and silica (Si), and total alkalinity (ALK). Other variables are initialized with observed vertical profiles or assumed small constant concentrations. For this second class of variables we imposed homogeneous von-Neumann boundary conditions. There is a surface flux of CO_2 following the OCMIP formulae (Sarmiento et al., 2000). During EIFEX on February 12 and February 26, 2004, 9 tons of iron solution, corresponding to 1.755 tons of pure iron each, were injected into the surface layer in an approximately circular area of 170 and 740 km^2, respectively, over 24 hours. In the model the fertilization is implemented as follows: on each of the corresponding (model-) dates, 1.755 tons of the pure iron are applied to 12 grid points (approximately 160 km^2) in the center of the eddy at a constant rate over a 24 hours period.

5.3.1. Simulating the bloom

The iron fertilization in both field experiment and numerical model induce a phytoplankton bloom that is monitored for 38 days. Figure 8 shows the simulated surface chlorophyll on selected days, overlaid by normalized LIDAR-derived fluorescence (Cembella et al., 2005). While the LIDAR-measurements are difficult to interpret quantitatively, they give an idea of the location of the chlorophyll patch. The agreement of modeled and observed patch locations confirms the success of the physical state estimation of Section 4.2 by independent observations.

Figure 9 compares vertical integrals of the observed chlorophyll *a* and POC concentration in the center of the fertilized patch and outside the patch (but within the eddy, i.e. following the “inpatch/outpatch” definition of Smetacek et al., 2012) with the corresponding simulated concentration (black lines). In the model, the patch is defined as the area where either the surface concentration of iron is above $0.15\,\mu\mathrm{mol\,m^{-3}}$ or the surface concentrations of iron and chlorophyll are above $0.08\,\mu\mathrm{mol\,m^{-3}}$ and $1\,\mathrm{mg\,m^{-3}}$; the eddy area is approximated based on simulated surface temperature and salinity fields. The chlorophyll *a* concentrations outside the patch remain at their initial value as observed, but the model solutions tends to overestimate

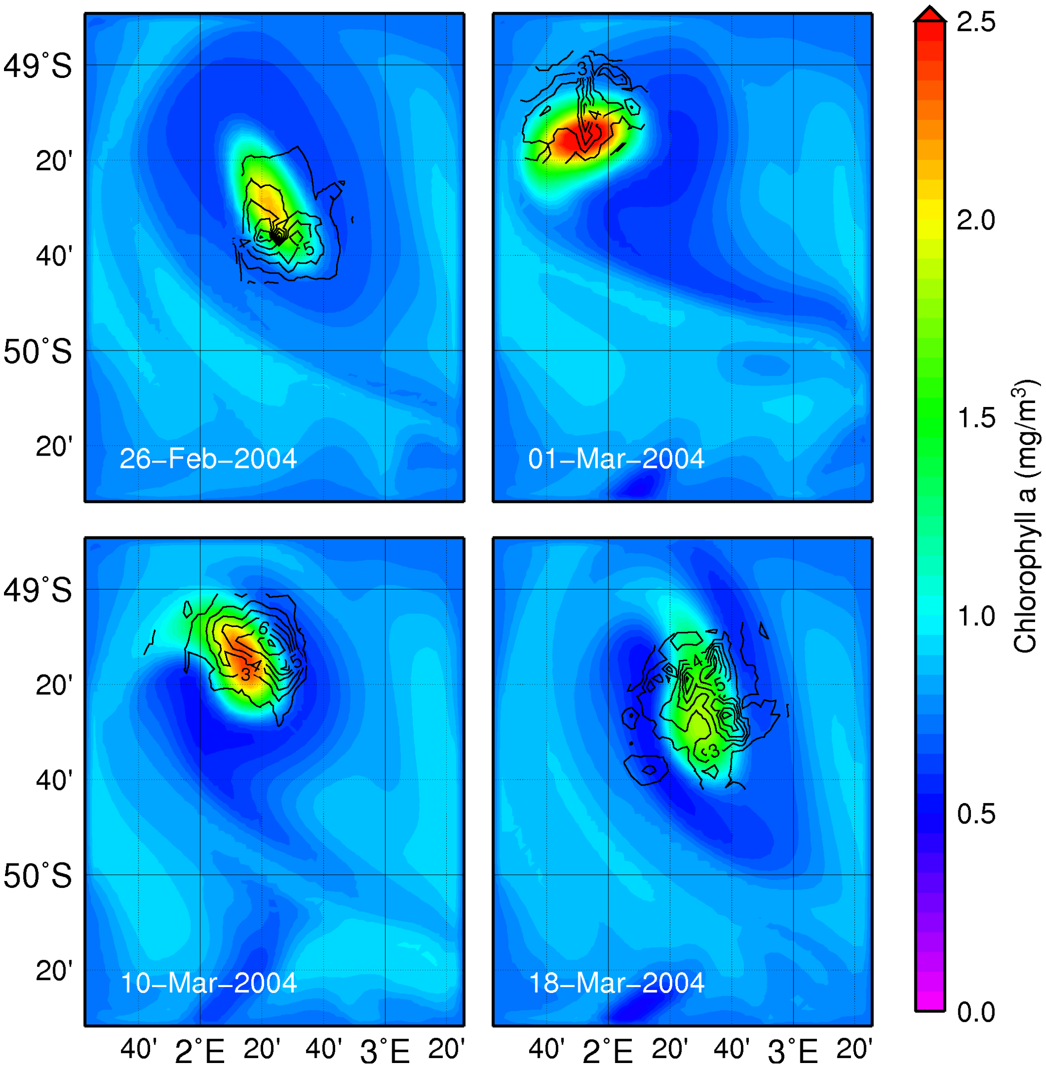

Figure 8: Modeled surface chlorophyll concentration (in $\mathrm{mg\,m^{-3}}$) on selected days (14, 18, 27, and 35 days after fertilization). Overlaid contours are normalized LIDAR-derived fluorescence giving an impression of the observed bloom location. Note that one revolution of the patch within the eddy (observed and simulated) took 7–10 days to complete.

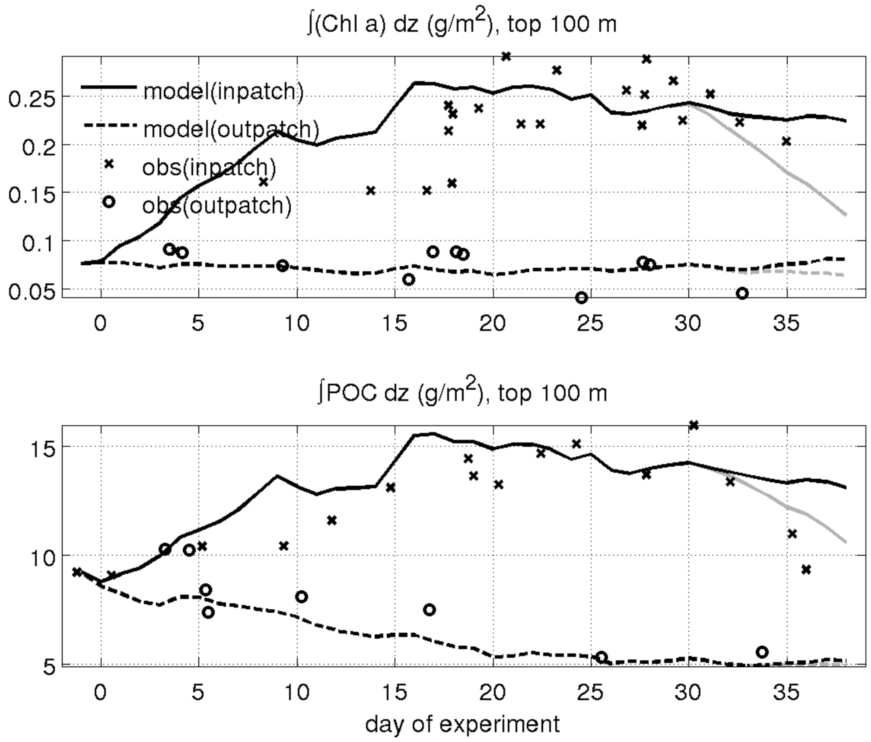

Figure 9: Integral over the top 100 m of observed (crosses and circles) and modeled (solid and dashed lines) chlorophyll *a* (gChl m^{-2}) and POC (gC m^{-2}) concentrations inside and outside of the fertilized patch. Grey lines refer to the experiment with increased aggregation (Eq. 7).

the chlorophyll *a* concentrations inside the patch during the beginning of the bloom. This early increase of simulated chlorophyll can be attributed to an artifact of the original Geider-model (Smith and Yamanaka, 2007). Sampling strategies could also have lead to low vertical integrals of chlorophyll *a*, as during this period the apparent variability of the mixed layer depth was higher than the sampling rate (see Smetacek et al., 2012, their Figure 2a). The parameterization of the iron uptake and utilization may be an additional reason for the fast rising concentrations. This parameterization assumes that the physiological activity is a function of the ambient dissolved iron concentration, while it should be the concentration within the phytoplankton cell. The uptake of iron by the cell introduces a delay of the onset of the bloom (Geider and La Roche, 1994, Peloquin and Smith Jr., 2006, Denman et al., 2006) that is not modeled.

The simulated build-up of particulate organic carbon (POC) inside the patch appears realistic, but its observed decrease after day 30 of the experiment is not reproduced properly. The almost linear decrease of POC outside the patch is slightly overestimated by the model. Both problems are likely related to the sinking parameterization (Eq.6). In a test with a constant sinking velocity of zero the POC concentrations outside the patch fit the observed concentrations much better (not shown), but this scenario with no gravitational sinking requires phytoplankton aggregation to be negligible and leads to no vertical flux of carbon (see below). Further, the model system may initially not be in steady state and the drop can be attributed to adjustment processes in the model due to inappropriate initial conditions for some of the unobserved model variables such as detritus.

Inside the patch, the modeled aggregation is not strong enough to make POC sink as observed. Therefore, the aggregates concentration in eq. (6) is increased in a second experiment by a time dependent factor

$$h_{\text{agg}} = \begin{cases} 1 & \text{for } t \leq t_0 \\ 1 + 0.25 \cdot [t - t_0]) & \text{for } t > t_0 \end{cases} \tag{7}$$

with $t_0 = 29$ days in order to increase the flux of phytoplankton into detritus and to accelerate the sinking of material towards the end of the bloom. With this parameterization we roughly represent the time-dependent formation of detritus that is expected from senescence of the bloom (Kahl et al., 2008). The grey lines in Figure 9 show that as a result of this time dependent factor both chlorophyll and POC drop towards the end of the experiment (but the POC decrease is still smaller than in the observations).

The POC evolution (Figure 10) is explored further by comparing the POC standing stocks in layers of 100 m thickness as in Smetacek et al. (2012), their Figure 4, to POC inferred from transmissometer measurements (dots in Figure 10). The modeled POC in the patch center (dashed line in Figure 10, reproduced from Figure 9) is very similar to the transmissometer measurements (dots in Figure 10). As expected, the patch averaged POC is generally lower. The model simulates most of the increase of POC in sub-surface layers towards the end of the experiment, but there is a spurious reduction and then a sudden increase in POC during the first half of the simulation period. We attribute this development to possibly inappropriate (because unknown) initial conditions for detritus and to subsequent adjustment processes. The tendency to underestimate the increase in POC below 200 m compared to the transmissometer data suggests that remineralization is too strong in the model or that sinking velocities are too high.

5.3.2. Export fluxes

Figure 11 shows the time averaged and horizontally averaged vertical carbon flux (with increased aggregation according to Eq. 7) underneath the

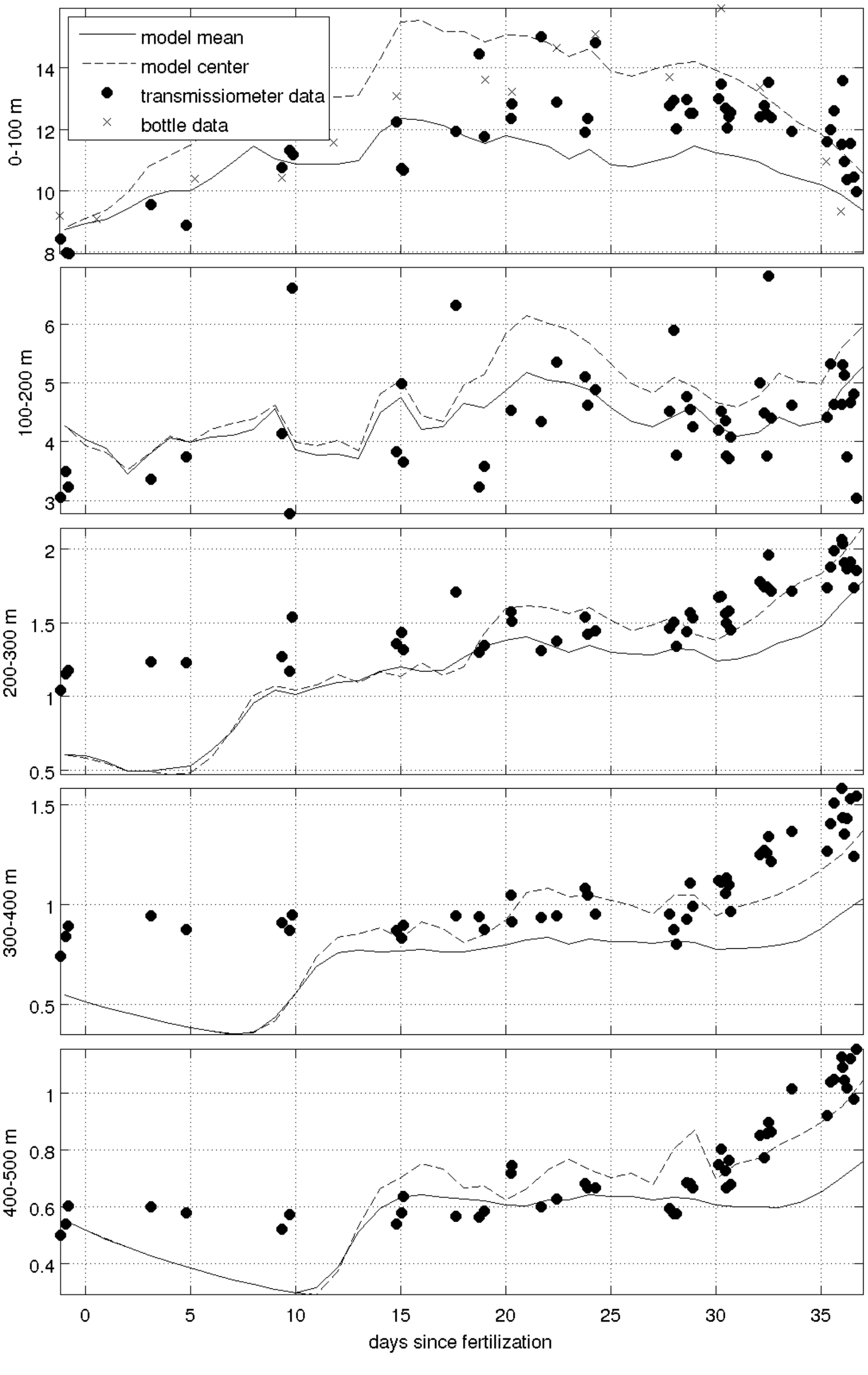

Figure 10: Comparison of modeled particulate organic carbon (POC, in $\mathrm{gC\,m^{-2}}$) and inferred POC from transmissometer observations (compare to Smetacek et al., 2012, Fig 4) per 100 m layers. The dashed line (same as grey line of Figure 9) corresponds to the POC at the position of the maximum surface chlorophyll *a* concentration and corresponds to the "hot spot" of Smetacek et al. (2012). The solid line is the mean over the patch. This mean is the basis of all estimates of export.

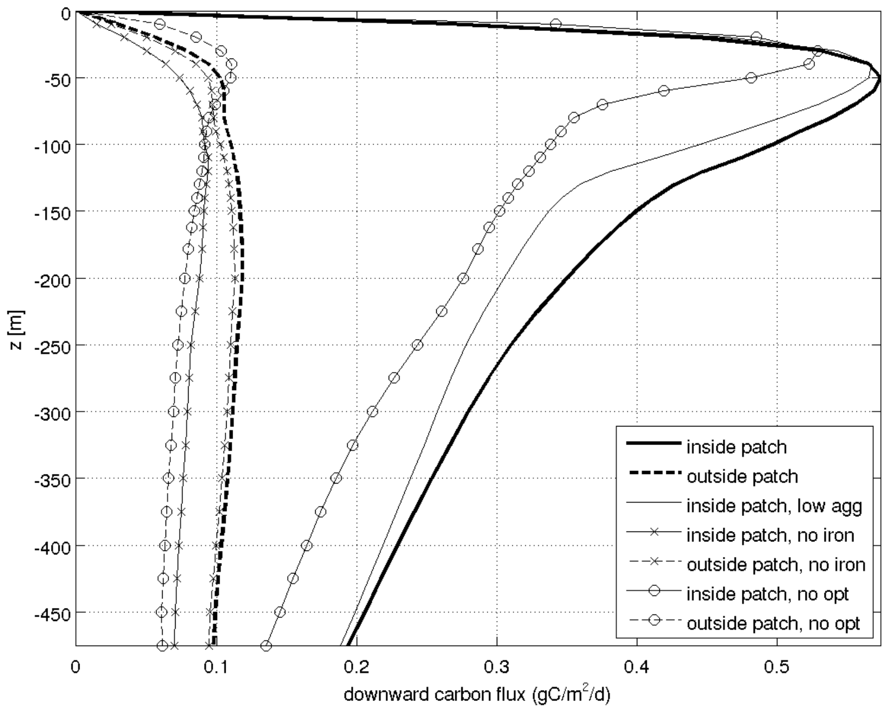

Figure 11: Horizontally averaged downward flux of carbon (in gC m^{-2} d^{-1}), averaged over day 30 through 39 of the experiments. Thick lines: experiment with iron fertilization and increased aggregate concentration; thin lines with crosses: experiment without iron fertilization; thin lines with open circles: experiment with iron fertilization but prior to optimization of physics. The thin grey line indicates the experiment with the original aggregation (Eq. 6).

fertilized patch and outside the fertilized patch (i.e. in the remaining part of the model domain) for the experiment with iron fertilization (thick lines) and for one without (thin lines with crosses). The time averaging period spans the last ten days of the experiment. In the mixed layer (above 100 m depth, see Figures 2 and 6), the vertical flux of carbon is governed by vertical mixing (as parameterized by the KPP mixing scheme) and the vertical gradient of POC. Below the mixed layer (starting around 150 m depth), the flux is determined by sinking detritus with settling velocities that increase with depth (see Eq. (6)) and by remineralization of detritus. Inside the patch, the vertical flux of carbon decreases from 0.4 gC m^{-2}d^{-1} at 150 m to below 0.2 gC m^{-2}d^{-1} at 500 m (bottom of the domain) implying that 50% of the exported carbon is remineralized before reaching 500 m. Outside the patch, there is a slight increase of vertical flux between the experiment with and without iron fertilization. This increase is attributed to the vertical shear of horizontal velocities, so that sinking particles are "left behind" by the patch when they enter depths with lower horizontal velocities. This effect is small in our simulation because of the small vertical shear. With lower aggregation (grey line) the export out of the mixed layer is smaller (approximately $0.33\ \mathrm{gC\,m^{-2}d^{-1}}$ at 150 m).

Figure 11 also shows the vertical carbon fluxes from a run with non-optimized physics (thin lines with open circles). Clearly, optimizing the physical trajectory has a strong effect on the vertical carbon flux. In the run without optimized physics, the maximum downward flux of carbon within the mixed layer is smaller than with the results of the state estimation. The shallow mixed layer depth in the former run (see Figure 4) is also reflected in a smaller vertical carbon flux at depths between 50 and 150 m. Below 150 m the vertical flux is dominated by sinking of detritus and, thus, the details of the flow field have a smaller impact, but the export from the mixed layer is small.

Jacquet et al. (2008) estimate low remineralization of about $13 \pm 1.4\%$ for EIFEX between 150 m and 1000 m. In the model, the estimated remineralization is much higher, but depends on both remineralization rates (see appendix) and sinking velocities. To explore the effect of the largely unconstrained sinking velocity further, the vertical flux of carbon is plotted in Figure 12 (black lines) for different sinking velocities of detritus (grey lines) as a function of parameter a in Eq. (6). Below the mixed layer, the flux generally decreases with depth because part of the detritus is lost by remineralization during the passage. Increasing the factor a reduces this loss because detritus sinks faster through the domain. In this way the export below 500 m depth can be increased up to 2.5 times by a 20-fold larger a that results in a 10-fold increase in sinking velocity. For $a = 5\,\mathrm{d^{-1}}$, as used in this study, the sinking velocity is already on the order of $100\,\mathrm{m\,d^{-1}}$, but the net remineralization decreases from 50% to 17% for $a = 100\,\mathrm{d^{-1}}$ (implying sinking velocities of order $1000\,\mathrm{m\,d^{-1}}$). While high settling speeds are plausible for large aggregates formed in the center of the patch (where plankton biomass was highest) and towards the end of the bloom (Smetacek et al., 2012), averaged effective sinking speeds are expected to be lower for the whole patch. For comparison, Jouandet et al. (2011) report sinking speeds estimated with indirect methods of up to $200\,\mathrm{m\,d^{-1}}$ in natural iron fertilization experiments. Decreasing the parameters of remineralization rates (see appendix) did not improve the solution (not shown). Vertical carbon fluxes outside the fertilized patch are not greatly affected by the vertical sinking velocity of detritus (not shown).

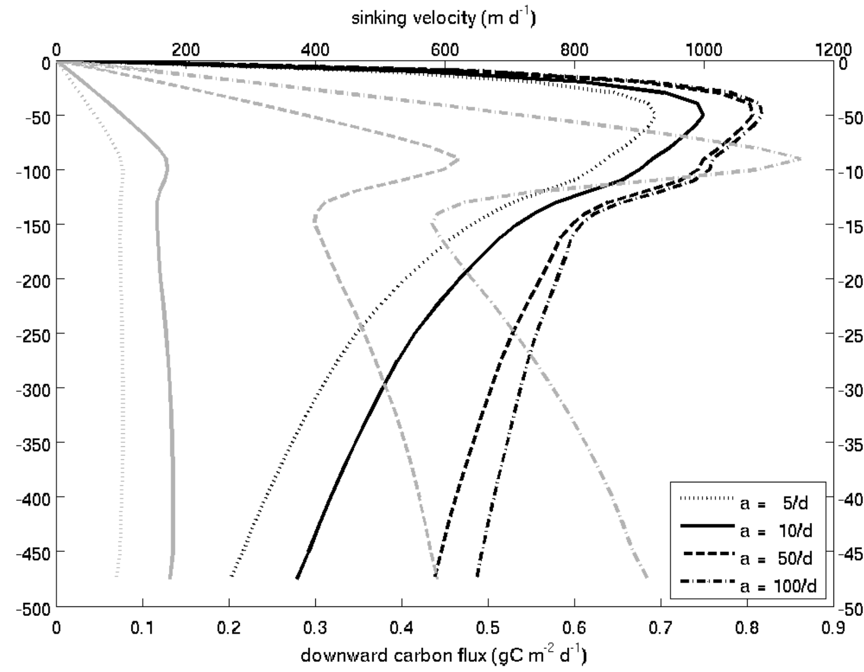

Figure 12: Horizontally averaged sinking velocities (in $\mathrm{m\,d^{-1}}$, grey lines) and the associated horizontally averaged downward flux of carbon (in $\mathrm{gC\,m^{-2}\,d^{-1}}$, black lines) in the fertilized patch as a function of parameter a in Eq. (6), averaged over day 30 through 39 of experiment.

5.3.3. Effect of iron fertilization

We can now go beyond the possibilities of a field experiment and repeat the exact simulation without the addition of iron. By subtracting this experiment from the run with iron fertilization we can estimate how much of the observed bloom may be attributed to the fertilization. Further, this technique reduces possible model biases that are independent of the iron fertilization; for example, the overly strong decrease of POC outside the patch (Figure 9) cancels out in such an experiment. Figure 13 shows estimates of fertilization-induced, vertically integrated carbon, silica, and nitrogen consumption from the nutrient difference of experiments with and without iron fertilization. The DIC difference (ΔDIC) between runs without and with iron fertilization, integrated to 100 m depth, peaks at $14.3\,\mathrm{gC\,m^{-2}}$. This amounts to a total of 16,700 t of DIC uptake due to iron fertilization in the upper 100 m in the entire model domain area of $29{,}300\,\mathrm{km^2}$. The peak value increases to $18.6\,\mathrm{gC\,m^{-2}}$ (and the net value to 20,700 t) when the difference is

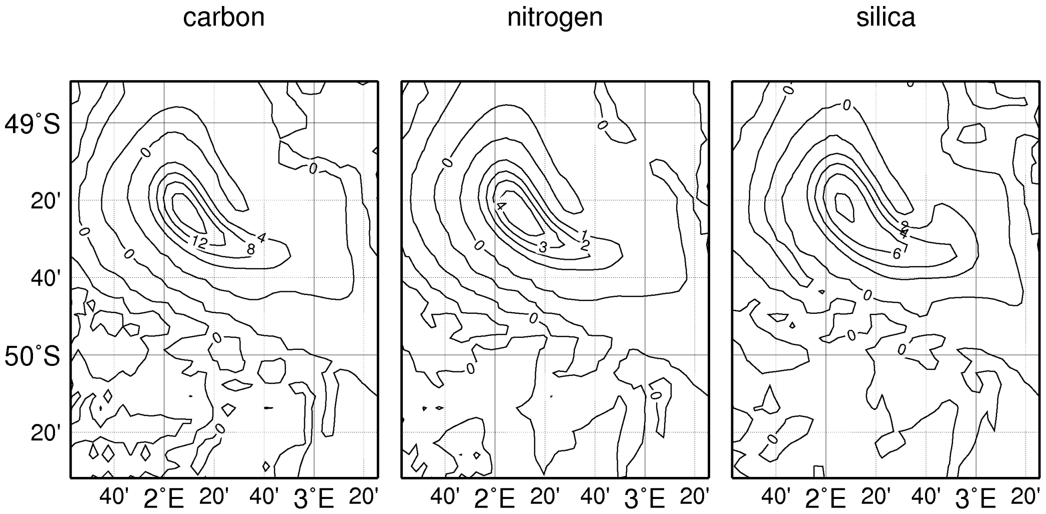

Figure 13: Estimated carbon, nitrogen, and silica consumption through biological activity induced by iron fertilization: vertical integral of the difference of nutrients at the end of the integration for experiments without and with iron fertilization. Contour interval is 4 gC m^{-2} for carbon, 1 gN m^{-2} for nitrogen, and 2 gSi m^{-2} for silica.

integrated to the bottom of the domain at 500 m (as shown in Figure 13).

To estimate the sensitivity of the carbon uptake to model parameterization, we tested variable sinking velocities. Using sinking speed parameters a of 10, 50, and 100 d^{-1} (Eq. (6)), the peak consumption of DIC in the upper 100 m increases by 0.7, 1.5, and 1.8 gC m^{-2} corresponding to an increase in carbon uptake by 1500 to 3500 t. This leads to an uncertainty of about 10–20% due to the unconstrained sinking velocity.

The particulate organic carbon (POC, in our model expressed as the sum of carbon in phytoplankton, zooplankton, and detritus) increases with iron fertilization by ΔPOC $\approx$ 9100 t in the top 100 m and by 15,000 t in the entire domain. The difference with ΔDIC (7600 and 5500 t) gives the carbon export out of the top 100 m and 500 m under the assumption that no (or only very little) POC has left the domain over the lateral open boundaries. This translates into a C/Fe export mass efficiency of 7600 t/(3.5 t) $\approx$ 2200 g/g $\approx$ 10,000 mol/mol and 5500 t/(3.5 t) $\approx$ 1600 g/g $\approx$ 7300 mol/mol. These numbers are lower limits, because not all of the iron (two fertilizations with 1.755 t each $\approx$ 3.5 t) is used in the experiment. The net iron utilization during the bloom in the experiments (including scavenged iron) is estimated as the difference of all dissolved iron at the end and iron at the beginning plus the iron released during the experiment as 13.4 t $-$ (8.5 t $+$ 3.5 t) $\approx$ 1.4 t. With this number for the iron input the C/Fe-efficiency increases to 5400 g/g (25,000 mol/mol) and 4000 g/g (18,000 mol/mol) for the top 100 m and for the entire domain down to 500 m. de Baar et al. (2005) report molar DIC/Fe uptake efficiencies in the range of 1066 to nearly 40,000, although the mean over different experiments was approximately 5600. According to de Baar et al. (2005), approximately 50% of the DIC uptake is converted to POC. Smetacek et al. (2012) estimate a molar DIC uptake efficiency of 13,000 for EIFEX. Our model estimates suggest that values from Smetacek et al. (2012) are strongly conservative as they assume no iron scavenging.

With the model we can also directly assess the net carbon export through the bottom of the domain by collecting the carbon that sinks out. In the run with iron fertilization 67,000 t of carbon have left the domain through the bottom (north of 50° S) by the end of the integration, but only 3,800 t are due to the iron fertilization (from the difference between runs with and without iron fertilization). This suggests that the above method based on budgets tends to overestimate the actual carbon export below 500 m, but note that the model tends to underestimate the net export inside the patch and overestimate it outside the patch (cf. Figure 9). Some of the difference between ΔPOC and ΔDIC can be explained by flux across the open boundaries.

Figure 14 shows the modeled POC per unit area above and below 150 m. As in Figure 9, the numbers represent averages over the entire patch, which again is defined as the area where the surface concentration of iron is above $0.15\,\mu\mathrm{mol\,m^{-3}}$ or where the surface concentrations of iron and chlorophyll are above $0.08\,\mu\mathrm{mol\,m^{-3}}$ and $1\,\mathrm{mmol\,m^{-3}}$. Also shown is the cumulative amount of POC exported through the bottom of the domain (at 500 m) below the patch. The top figure shows that POC builds up in the top 150 m of the water column until about day 15 (see also Figure 9). Then POC sinks, mostly through layer 150–500 m (because this layer does not accumulate POC) to depths below 500 m (out of the domain). The overall export out of the domain is $3.7\,\mathrm{gC\,m^{-2}}$. Assuming no POC production below the mixed layer we can use the budgets of Figure 14 (top panel) to estimate an export of $9.1\,\mathrm{gC\,m^{-2}}$ below 150 m and similarly $12.6\,\mathrm{gC\,m^{-2}}$ below 100 m (from repeating the calculation that lead to Figure 14 with different depth ranges, see also Figure 10). Smetacek et al. (2012) estimate an export production due to iron fertilization from the difference in DIC and POC concentrations before and after the bloom in the top 100 m of $14.4 \pm 4.8\,\mathrm{gC\,m^{-2}}$ during days 24 to 36 since the fertilization. With their background flux estimates of $6 \pm 4\,\mathrm{gC\,m^{-2}}$ this adds up to about $20\,\mathrm{gC\,m^{-2}}$. The model estimate is about 40% lower, consistent with the lower drop in near surface POC compared to observations in Figure 9. The net POC-flux for the entire period (days 0–36) is estimated from ^{234}Thorium depletion data as $16.7\,\mathrm{gC\,m^{-2}}$ (from integrating Figure S5.1 of Smetacek et al., 2012).

The difference in POC content between runs with and without iron fertil-

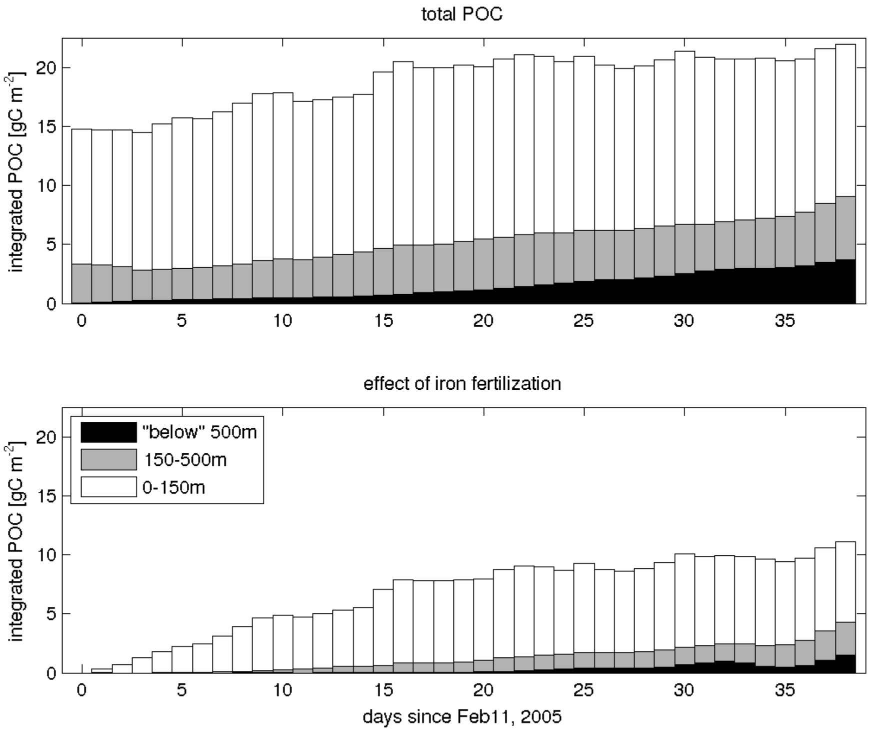

Figure 14: Modeled particulate organic carbon (POC) below and above 150 m depth averaged over the patch. "Below" 500 m refers to POC that sank out of the domain. Top: POC of experiment with iron fertilization, bottom: difference of experiments with and without iron fertilization.

ization in the bottom panel of Figure 14 shows that in the model simulation only 1.5 gC m^{-2} of the POC exported below 500 m is actually induced by iron fertilization. Smetacek et al. (2012) find, based on transmissometry, an increase in flux of 8.4 gC m^{-2} below 500m below a "hot-spot" within the patch. For the depths 150 m and 100 m the corresponding model values are 4.3 gC m^{-2} and 6.0 gC m^{-2}. The latter is only 40% of the 14.44±4.8 gC m^{-2} due to fertilization of Smetacek et al. (2012) but comparable to ^{234}Thorium-based estimates of 7.8 gC m^{-2} of POC-export out of the top 100 m for the last 12 days of the experiment. Concurrent with the discrepancies with Smetacek et al. (2012)'s estimate, we simulate with the model that the export decreases strongly with depth, and the export at 500 m is only 12% of that at 100 m.

6. Conclusions

Modern state estimation techniques are a powerful tool for the analysis of observational data. In particular, the dynamics of numerical models can be used to consistently interpolate between observations. In our case the solution is mostly controlled by the open boundaries, and to a smaller extent by initial conditions.

In the context of the EIFEX data set in combination with a numerical model (MITgcm+REcoM), the strong influence of the physical environment on biogeochemical processes emerges as a fundamental result. In the optimized simulation, the mixed layer depth is deeper (and thus more realistic) than without optimization and the horizontal position of the eddy is corrected with respect to the first guess estimate. In spite of the generally deeper mixed layer (i.e. less available light), the export flux is larger with optimized physics, also suggesting that the light parameterization within REcoM is appropriate. We argue, that (unrealistically) strong vertical velocities, associated with spurious divergent flow due to the open boundary conditions—and the (largely unconstrained) nutrient flux across the open boundaries, affect the un-optimized solution because the core of the eddy and the fertilized patch are much closer to the northern boundary than in the optimized case. In the optimized case, the fertilized patch moved along with the core of the eddy to the correct position. Thus, the patch is never directly affected by the open boundaries and the biogeochemical simulation improves.

Further, changing important parameters in the ecosystem model, such as the vertical sinking velocity, can have a similarly strong impact on vertical carbon flux estimates as the flow field. Smetacek et al. (2012) postulated high sinking rates of more than $500\,\mathrm{m\,d^{-1}}$ and aggregates in the centimeter size range to explain observed POC increases in the entire water column underneath the so-called “hot-spot” within the fertilized patch, but infer much lower settling speeds outside this “hot-spot”. Increasing the vertical sinking velocities in the model from $100\,\mathrm{m\,d^{-1}}$ to $800\,\mathrm{m\,d^{-1}}$ increases the deep export by a factor 2.5 at 500 m depth. While this factor reduces the difference to the *in-situ* export estimate by Smetacek et al. (2012), the high effective sinking velocities appear excessive (McDonnell and Buesseler, 2010, Iversen et al., 2010, Jouandet et al., 2011) indicating that remineralization rates below the mixed layer are too high in the numerical model to allow larger deep export (compare also with Jacquet et al., 2008).

Tuning an ecosystem model systematically requires non-linear parameter estimation techniques (e.g., Schartau and Oschlies, 2003). We have postponed this exercise and have used subjective tuning of model parameters to achieve an ecosystem trajectory that reproduces most of the observed characteristics of the phytoplankton bloom during the European iron fertilization experiment EIFEX.

Based on the best estimate of the flow field and the temporal evolution of biogeochemical parameters during the open ocean experiment EIFEX, the numerical modeling approach allows to investigate experimental configurations that could not have been carried out in the field. Comparing model simulations with and without iron fertilization gives an independent estimate of the impact of iron fertilization on the export of POC. The model simulation is largely consistent with observations of chlorophyll *a* and particular organic matter (we only showed POC). However, our estimates of export flux at 100 m are about 40% lower than Smetacek et al. (2012)'s estimates. Consequently, we find smaller effects of iron fertilization on vertical fluxes.

The difference between Smetacek et al. (2012)'s and our estimates can have many reasons. First of all, the definition of the patch area is somewhat arbitrary and different area averages immediately give different results. To that end, Smetacek et al. (2012)'s estimates all refer to a "hot-spot" within the patch whereas our estimates are based on averages over the entire patch. Further, even when comparing maximum values in the modeled patch to the "hot-spot" of Smetacek et al. (2012) our model underestimates the decrease in surface POC and hence vertical fluxes in this area. Finally, physical processes in the model are dynamic while budgets in Smetacek et al. (2012) were based on the available estimates of lateral and vertical mixing, which tend to represent spatial or temporal averages.

The numerical model used here (most likely) does not describe the complete state of the system during EIFEX, so that the model based estimates contain errors that are difficult to estimate. The EIFEX bloom terminated with a very abrupt export event that cannot be reproduced by REcoM without arbitrary tuning (see Eq. 7). Also, in our method of taking the difference between two model runs, model errors play an important role. From simple sensitivity experiments we can provide a rough error estimate for the figures of 10–20%. We estimate an iron induced DIC uptake of $10.5\,\mathrm{gC\,m^{-2}}$ and an accumulation of POC of $5.1\,\mathrm{gC\,m^{-2}}$ in the top 100 m. For this layer, Smetacek et al. (2012) estimate a slightly higher DIC uptake of $13.2\pm1.2\,\mathrm{gC\,m^{-2}}$ and a much lower POC accumulation of $1.3\pm0.8\,\mathrm{gC\,m^{-2}}$. The decrease of POC towards the end of the experiment is not accurately simulated by the model, so that our export estimates may to be too low for that reason alone. Instead, most of the POC anomaly that builds up after iron fertilization stays in the upper 150 m of the water column implying that in the numerical model, in spite of the explicit increase of sinking in Eq. (7), the increase of POC in the surface layers is not balanced by a strongly increased vertical export so that the deep export does not even double under iron fertilization. This indicates a requirement for further improvements to the vertical sinking parameterization (6) for particulate organic matter. The simulated decrease of POC outside the fertilized patch overestimates the observed development and one can argue that the numerical model overestimates the export under unperturbed conditions. We removed this bias by analysing the differences between perturbed (with iron fertilization) and unperturbed experiments, essentially assuming a linear effect of the perturbation. To what extent this assumption is valid remains unclear. Improving the ecosystem model to achieve a closer model-data fit is necessary and will be the subject of a different paper.

Acknowledgements. The authors thank Patrick Heimbach for indispensable help with the adjoint model and the ECCO infrastructure; Gert König-Langlo for providing the meteorological data through the Meteorological Information System at AWI (MISAWI); Christoph Völker and Sönke Hohn for help in tuning and modifying the ecosystem model; Marc Taylor for critical comments on the manuscript; we thank all participants of the EIFEX cruise for supplying generously their data in support of this work. Geographic maps were drawn with the Generic Mapping Tools (Wessel and Smith, 1998).

Appendix A. A Regulated Ecosystem Model (REcoM) with Silica and Iron

Here we describe the equations of the ecosystem model REcoM (Schartau et al., 2007, Hohn, 2009), as they are used in this study. REcoM is a series of ecosystem models that contain an identical basic kernel. For this study it has been augmented with silica and iron to represent diatom dominated communities (REcoM&Dia).

Appendix A.1. State variables and equations

REcoM&Dia has 16 state variables in the current configuration. They are listed in Table A.2. The variables are divided into five different compounds. With the abbreviation $q = P_N/P_C$ and $q^{Si} = P_{Si}/P_N$ the source-minus-sink terms S_A for the different groups are

Table A.2: REcoM&Dia state variables and their abbreviations.

DIC	dissolved inorganic carbon (TCO_2)
DIN	dissolved inorganic nitrogen
Si	dissolved inorganic silicate
P_N	nitrogen in phytoplankton
P_C	carbon in phytoplankton
P_{Si}	silicate in phytoplankton
Z_N	nitrogen in heterotrophic zooplankton
Z_C	carbon in heterotrophic zooplankton
DON	dissolved organic nitrogen
EOC	extracellular organic carbon
D_N	nitrate in detritus
D_C	carbon in detritus
D_{Si}	silicate in detritus
Fe	silicate in phytoplankton
Chl	chlorophyll a concentration
ALK	alkalinity

1. Dissolved inorganic compounds:

$$\begin{aligned} S_A\,(DIC) = {} & (r_{phy} - C_{phot})\,P_C \\ & + \rho_C(T)\,EOC \\ & + r_{zoo}\,Z_C \end{aligned} \tag{A.1}$$

$$S_A\,(DIN) = -\frac{V_C^N}{q}\,P_N + \rho_N(T)\,DON \tag{A.2}$$

$$\begin{aligned} S_A\,(ALK) = {} & \left(\frac{1}{16} + 1\right) \\ & \cdot \left(\frac{V_C^N}{q}\,P_N - \rho_N(T)\,DON\right) \end{aligned} \tag{A.3}$$

$$S_A\,(Si) = -V_C^{Si}\,P_C + \omega_{Si}(T)\,D_{Si} \tag{A.4}$$

$$S_A\,(Fe) = q^{Fe}\,S_A\,(DIC) - k_{sc}\,Fe' \tag{A.5}$$

Table A.3: REcoM parameter names and values in the current application

Name	Units	Symbol	value
maximal N/C-cell quota	$\mathrm{mmol\,N/mmol\,C}$	q_{max}	0.2
minimal N/C-cell quota	$\mathrm{mmol\,N/mmol\,C}$	q_{min}	0.04
minimal Si/C-cell quota	$\mathrm{mmol\,Si/mmol\,C}$	q_{min}^{Si}	0.0408
maximal Si/C-cell quota	$\mathrm{mmol\,Si/mmol\,C}$	q_{max}^{Si}	0.8
N/C-uptake ratio	$\mathrm{mmol\,N/mmol\,C}$	q_U	0.2
Si/C-uptake ratio	$\mathrm{mmol\,Si/mmol\,C}$	q_U^{Si}	0.204
Maximum chlorophyll *a* to nitrogen ratio	$\mathrm{g\,CHL\,(mol\,N)^{-1}}$	q_{max}^{Chl}	2.5
iron to carbon ratio	$\mu\mathrm{mol\,Fe/mmol\,C}$	q^{Fe}	0.005
Redfield ratio	$\mathrm{mmol\,C/mmol\,N}$	R	6.625
attenuation coefficient for water	$\mathrm{m^{-1}}$	k_w	0.04
chlorophyll-specific attenuation coefficients	$\mathrm{m^{-1}\,(mg\,Chl)^{-1}}$	a_{CHL}	0.03
chlorophyll-specific initial slope of P-I curve	$\frac{\mathrm{molC}}{\mathrm{g\,Chl}}\,\mathrm{(W\,m^{-2}\,d)^{-1}}$	α	0.2
maximum of C-specific rate of photosynthesis	$\mathrm{d^{-1}}$	p^*_{max}	4.0
Cost of biosynthesis	$\mathrm{mmol\,C/mmol\,N}$	b	2.0
Cost of biosynthesis	$\mathrm{mmol\,C/mmol\,Si}$	b_{Si}	1.0
Half saturation constant (nitrogen)	$\mathrm{mmol\,N\,m^{-3}}$	k_{DIN}	0.55
Half saturation constant (silicium)	$\mathrm{mmol\,Si\,m^{-3}}$	k_{Si}	4.0
Half saturation constant (iron)	$\mu\mathrm{mol\,Fe\,m^{-3}}$	k_{Fe}	0.12
Constant respiration rate of phytoplankton	$\mathrm{d^{-1}}$	r^*_{phy}	0.01
aggregation	$\mathrm{(mmol\,N\,m^{-3})^{-1}}$	a_{PP}	0.02
aggregation	$\mathrm{(mmol\,N\,m^{-3})^{-1}}$	a_{PD}	0.22
Phytoplankton loss/mortality/excudation	$\mathrm{d^{-1}}$	γ_C	0.1
Phytoplankton loss/mortality/excudation	$\mathrm{d^{-1}}$	γ_N	0.05
degradation of chlorophyll	$\mathrm{d^{-1}}$	γ_{chl}	0.01
maximum zooplankton grazing rate	$\mathrm{d^{-1}}$	g_{max}	0.5
Grazing half saturation constant	$\mathrm{(mmol\,N\,m^{-3})^2}$	ϵ	20.0
Zooplankton mortality	$\mathrm{d^{-1}}$	Φ_z	0.05
Zooplankton respiration time scale	d	τ_r	1.0
DON degradation rate	$\mathrm{d^{-1}}$	ρ^*_N	0.05
EOC degradation rate	$\mathrm{d^{-1}}$	ρ^*_C	0.004
Detritus remineralization rate (Nitrogen)	$\mathrm{d^{-1}}$	ω^*_N	0.01
Detritus remineralization rate (Carbon)	$\mathrm{d^{-1}}$	ω^*_C	0.1
Maximal remineralization rate (Silicium)	$\mathrm{d^{-1}}$	ω^*_{Si}	0.02
Iron scavenging rate	$\mathrm{d^{-1}}$	k_{sc}^{Fe}	0.25
Total ligand	$\mu\mathrm{mol\,m^{-3}}$	L_T	1.0
Conditional stability constant	$(\mu\mathrm{mol\,m^{-3}})^{-2}$	K_{FeL}^{cond}	10.0
Phytoplankton sinking velocity	$\mathrm{m\,d^{-1}}$	w_P	0.0
Detritus sinking velocity	$\mathrm{m\,d^{-1}}$	w_D	*Eq.* (6)

2. Phytoplankton:

$$S_A\left(P_C\right) = \left(C_{phot} - r_{phy} - \gamma_C\right)\, P_C - \frac{1}{q}\, \left(\mathcal{G} + \mathcal{A}\right) - w_P\, \frac{\partial P_C}{\partial z} \tag{A.6}$$

$$S_A\left(P_N\right) = \frac{V_C^N}{q}\, P_N - \gamma_N\, P_N - \mathcal{G} - \mathcal{A} - w_P\, \frac{\partial P_N}{\partial z} \tag{A.7}$$

$$S_A\left(P_{Si}\right) = V_C^{Si}\, P_C - \frac{P_{Si}}{P_N}\, \left(\gamma_N\, P_N + \mathcal{G} + \mathcal{A}\right) - w_P\, \frac{\partial P_{Si}}{\partial z} \tag{A.8}$$

$$S_A\left(Chl\right) = \left(\mathcal{S}_{chl} - \gamma_{chl}\right)\, Chl - \frac{Chl}{P_N}\, \left(\mathcal{G} + \mathcal{A}\right) - w_P\, \frac{\partial Chl}{\partial z} \tag{A.9}$$

3. Zooplankton:

$$S_A\left(Z_C\right) = \frac{\mathcal{G}}{q} - r_{zoo}\, Z_C - \left(\Phi_z\, Z_N^2\right)\, \frac{Z_C}{Z_N} \tag{A.10}$$

$$S_A\left(Z_N\right) = \mathcal{G} - \Phi_z\, Z_N^2 \tag{A.11}$$

4. Detritus:

$$
\begin{aligned}
S_A\,(D_C) = {} & \frac{\mathcal{A}}{q} + \left(\Phi_z\, Z_N^2\right)\,\frac{Z_C}{Z_N} \\
& - \omega_C(T)\, D_C \\
& - w_D\, \frac{\partial D_C}{\partial z}
\end{aligned}
\tag{A.12}
$$

$$
\begin{aligned}
S_A\,(D_N) = {} & \mathcal{A} + \Phi_z\, Z_N^2 - \omega_N(T)\, D_N \\
& - w_D\, \frac{\partial D_N}{\partial z}
\end{aligned}
\tag{A.13}
$$

$$
\begin{aligned}
S_A\,(D_{Si}) = {} & \frac{P_{Si}}{P_N}\,(\mathcal{G} + \mathcal{A}) - \omega_{Si}(T)\, D_{Si} \\
& - w_D\, \frac{\partial D_{Si}}{\partial z}
\end{aligned}
\tag{A.14}
$$

5. Extracellular organic material (with organic nitrogen being completely dissolved):

$$
\begin{aligned}
S_A\,(EOC) = {} & \gamma_C\, P_C + \omega_C(T)\, D_C \\
& - \rho_C(T)\, EOC
\end{aligned}
\tag{A.15}
$$

$$
\begin{aligned}
S_A\,(DON) = {} & \gamma_N\, P_N + \omega_N(T)\, D_N \\
& - \rho_N(T)\, DON
\end{aligned}
\tag{A.16}
$$

Appendix A.2. Parameterizations

The above expressions involve the following parameterizations and limiting functions. A list of all model parameters and their values can be found in Table A.3.

- regulation term for photosynthesis

$$
\begin{aligned}
\mathcal{R}_{phot} = \min\Bigg(& F(q_{min}, q, 50), \\
& F(q_{min}^{Si}, q^{Si}, 1000), \\
& \frac{Fe}{k_{Fe} + Fe}\Bigg)
\end{aligned}
\tag{A.17}
$$

- maximal growth rate

$$
p_{max}^{C} = p_{max}^{*}\, f_{arr}(T)\, \mathcal{R}_{phot}
\tag{A.18}
$$

- Arrhenius temperature function

$$f_{arr}(\theta) = \exp\left(-4500\left(\frac{1}{\theta} - \frac{1}{\theta_{ref}}\right)\right) \tag{A.19}$$

- limiting function

$$F(a, b, s) = 1 - \exp\left(-s\ [|a-b| - (a-b)]^2\right) \tag{A.20}$$

- carbon assimilation, with $I(z)$ = photosynthetically available radiation (PAR)

$$C_{phot} = p^C_{max}\left\{1 - \exp\left(-\alpha\frac{I(z)}{p^C_{max}}\frac{Chl}{P_C}\right)\right\} \tag{A.21}$$

- maximum carbon specific N assimilation

$$V^N_{C,max} = 0.7\, p^C_{max}\, q_U F(q, q_{max}, 1000) \tag{A.22}$$

- carbon specific N assimilation of phytoplankton

$$V^N_C = V^N_{C,max}\frac{DIN}{k_{DIN} + DIN} \tag{A.23}$$

- maximum carbon specific Si assimilation

$$\begin{aligned} V^{Si}_{C,max} = {} & 0.7\, p^*_{max}\, f_{arr}(T) q^{Si}_U \\ & \cdot F(q, q_{max}, 1000) \\ & \cdot F(q^{Si}, q^{Si}_{max}, 1000) \end{aligned} \tag{A.24}$$

- carbon specific Si assimilation of phytoplankton

$$V^{Si}_C = V^{Si}_{C,max}\frac{Si}{k_{Si} + Si} \tag{A.25}$$

- chlorophyll synthesis

$$\mathcal{S}_{chl} = q^{Chl}_{max}\, V^N_C\ \min\left(1, \frac{C_{phot}}{\alpha\,\frac{Chl}{P_C}\, I(z)}\right) \tag{A.26}$$

- respiration of phytoplankton

$$r_{phy} = r^*_{phy} + b\, V_C^N + b_{Si}\, V_C^{Si} \tag{A.27}$$

- grazing flux

$$\mathcal{G} = g_{max} \frac{P_N^2}{\epsilon + P_N^2}\, Z_N \tag{A.28}$$

- zooplankton respiration

$$r_{zoo} = \tau_r^{-1} f_{arr}(T) \left(\frac{Z_C}{Z_N} - R \right) \tag{A.29}$$

- aggregation

$$\mathcal{A} = \left(a_{PD}\, D_N + a_{PP}\, P_N \right)\, P_N \tag{A.30}$$

- degradation rates of dissolved/extracellular organic matter

$$\rho_X(T) = f_{arr}(T)\, \rho_X^* \tag{A.31}$$

- detritus remineralization rates

$$\omega_X(T) = f_{arr}(T)\, \omega_X^* \tag{A.32}$$

- detritus remineralization rate (silica pool)

$$\begin{aligned} \omega_{Si}(T) = \min\Bigg(& \omega_{Si}^*, 1.32 \\ & \times 10^{16} \, \exp\left(-\frac{11200.0}{T} \right) \Bigg) \end{aligned} \tag{A.33}$$

- free iron Fe' is computed from

$$\begin{aligned} [Fe'] + [L'] & \underset{k_d}{\overset{k_f}{\rightleftharpoons}} [FeL] \\ [Fe] &= [Fe'] + [FeL] \\ [L_T] &= [L'] + [FeL] \\ K_{FeL}^{cond} &= \frac{[FeL]}{[Fe'][L']} \end{aligned} \tag{A.34}$$

following Parekh et al. (2004), where FeL is complexed iron associated with an organic ligand, L_T is the total ligand, assumed to be constant, L' is free ligand, and K_{FeL}^{cond} is the conditional stability constant when the system is in equilibrium.

- The photosynthetically available light is computed by integrating from the top, taking into account the attenuation of water k_w and chlorophyll $a_{CHL} \cdot Chl$ for a self-shading effect.

References

Ayoub, N., 2006. Estimation of boundary values in a North Atlantic circulation model using an adjoint method. Ocean Modelling 12 (3–4), 319–347.

Bennett, A. F., 2002. Inverse Modelling of the Ocean and Atmosphere. Cambridge University Press, Cambridge, UK.

Cembella, B., Rohr, H., Loquay, K.-D., Strass, V., 2005. Mapping horizontal spreading of a developed phytoplankton bloom using an airborne chlorophyll a fluorescence LIDAR. In: Smetacek et al. (2005), pp. 38–43.

Cisewski, B., Strass, V., Losch, M., Prandke, H., 2008. Mixed layer analysis of a mesoscale eddy in the Antarctic Polar Front Zone. J. Geophys. Res. 113 (C055017).

de Baar, H. J. W., Boyd, P. W., Coale, K. H., Landry, M. R., Tsuda, Atsushiand Assmy, P., Bakker, D. C. E., Bozec, Y., Barber, R. T., Brzezinski, M. A., Buesseler, K. O., Boyé, M., Croot, P. L., Gervais, F., Gorbunov, M. Y., Harrison, P. J., Hiscock, W. T., Laan, P., Lancelot, C., Law, C. S., Levasseur, M., Marchetti, A., Millero, F. J., Nishioka, J., Nojiri, Y., van Oijen, T., Riebesell, U., Rijkenberg, M. J. A., Saito, H., Takeda, S., Timmermans, K. R., Veldhuis, M. J. W., Waite, A. M., Wong, C.-S., 2005. Synthesis of iron fertilization experiments: From the Iron Age in the Age of Enlightenment. J. Geophys. Res. 110 (C9), C09S16.

Denman, K. L., Völker, C., Peña, A., Rivkin, R. B., 2006. Modelling the ecosystem response to iron fertilization in the subarctic NE Pacific: The influence of grazing and Si and N cycling on CO_2 drawdown. Deep-Sea Res. II 53, 2327–2352.

Dwivedi, S., Haine, T. W. N., Del Castillo, C. E., 2011. Upper ocean state estimation in the Southern Ocean Gas Exchange Experiment region using the four-dimensional variational technique. J. Geophys. Res. 116 (C00F02).

Ferreira, D., Marshall, J., Heimbach, P., 2005. Estimating eddy stresses by fitting dynamics to observations using a residual-mean ocean circulation model. J. Phys. Oceanogr. 35 (10), 1891–1910.

Gebbie, G., Heimbach, P., Wunsch, C., 2006. Strategies for nested and eddy-resolving state estimation. J. Geophys. Res. 111 (C10), C10073.
URL `http://dx.doi.org/10.1029/2005JC003094`

Geider, R. J., La Roche, J., 1994. Mini-review: The role of iron in phytoplankton photosynthesis, and the potential for iron-limitation of primary productivity in the sea. Photosynthesis Research 39 (3), 275–301.

Geider, R. J., MacIntyre, H. L., Kana, T. M., 1998. A dynamic regulatory model of phytoplanktonic acclimation to light, nutrients, and temperature. Limnol. Oceanogr. 43 (4), 679–694.

Giering, R., Kaminski, T., 1998. Recipes for adjoint code construction. ACM Trans. Math. Softw. 24 (4), 437–474.

Gilbert, J. C., Lemaréchal, C., 1989. Some numerical experiments with variable-storage quasi-Newton algorithms. Mathematical Programming 45, 407–435.

Heimbach, P., Hill, C., Giering, R., 2002. Automatic generation of efficient adjoint code for a parallel Navier-Stokes solver. In: J.J. Dongarra, P.M.A. Sloot and C.J.K. Tan (Ed.), Computational Science – ICCS 2002. Vol. 2331, part 3 of Lecture Notes in Computer Science. Springer-Verlag, Berlin (Germany), pp. 1019–1028.

Heimbach, P., Hill, C., Giering, R., 2005. An efficient exact adjoint of the parallel MIT general circulation model, generated via automatic differentiation. Future Generation Computer Systems (FGCS) 21 (8), 1356–1371.

Hibbert, A., Leach, H., Strass, V., Cisewski, B., 2009. Mixing in cyclonic eddies in the Antarctic Circumpolar Current. J. Mar. Res. 67 (1), 1–23.

Hohn, S., 2009. Coupling and decoupling of biogeochemical cycles in marine ecosystems. Ph.D. thesis, Bremen University.

Iversen, M. H., Nowald, N., Ploug, H., Jackson, G. A., Fischer, G., 2010. High resolution profiles of vertical particulate organic matter export off Cape Blanc, Mauritania: Degradation processes and ballasting effects. Deep-Sea Res. I 57 (6), 771–784.

Jacquet, S. H. M., Savoye, N., Dehairs, F., Strass, V. H., Cardinal, D., 2008. Mesopelagic carbon remineralization during the European Iron Fertilization Experiment. Global Biogeochem. Cycles 22 (1), GB1023.

Jouandet, M.-P., Trull, T. W., Guidi, L., Picheral, M., Ebersbach, F., Stemmann, L., Blain, S., 2011. Optical imaging of mesopelagic particles indicates deep carbon flux beneath a natural iron-fertilized bloom in the Southern Ocean. Limnol. Oceanogr. 56 (3), 1130–1140.

Kahl, L. A., Vardi, A., Schofield, O., 2008. Effects of phytoplankton physiology on export flux. Mar. Ecol. Prog. Ser. 354, 3–19.

Kivman, G., 2003. Sequential parameter estimation for stochastic systems. Nonlin. Proc. Geophys. 10, 253–259.

König-Langlo, G., Augstein, E., 1994. Parameterization of the downward long-wave radiation at the Earth's surface in polar regions. Meteor. Z. 3 (6), 343–347.

König-Langlo, G., Marx, B., 1997. The meteorological information system at the Alfred Wegener Instiute. In: Lautenschlager, M., Reinke, M. (Eds.), Climate and Environmental Database Systems. Kluwer Academic Publisher, Norwell, USA, pp. 117–126.

Kriest, I., Oschlies, A., 2008. On the treatment of particulate organic matter sinking in large-scale models of marine biogeochemical cycles. Biogeosciences 5, 55–72.
URL `http://www.biogeosciences.net/5/55/2008/`

Large, W. G., McWilliams, J. C., Doney, S. C., 1994. Oceanic vertical mixing: A review and a model with a nonlocal boundary layer parameterization. Rev. Geophys. 32 (4), 363–404.

Large, W. G., Pond, S., 1981. Open ocean momentum flux measurements in moderate to strong winds. J. Phys. Oceanogr. 11, 324–336.

Large, W. G., Pond, S., 1982. Sensible and latent heat flux measurements over the ocean. J. Phys. Oceanogr. 12, 464–482.

Lea, D. J., Haine, T. W. N., Gasparovic, R. F., 2006. Observability of the Irminger Sea circulation using variational data assimilation. Quart. J. Roy. Meteor. Soc.

Losch, M., Heimbach, P., 2007. Adjoint sensitivity of an ocean general circulation model to bottom topography. J. Phys. Oceanogr. 37 (2), 377–393.

Losch, M., Schröter, J., 2004. Estimating the circulation from hydrography and satellite altimetry in the Southern Ocean: Limitations imposed by the current geoid models. Deep-Sea Res. I 51 (9), 1131–1143.

Marshall, J., Adcroft, A., Hill, C., Perelman, L., Heisey, C., 1997. A finite-volume, incompressible Navier Stokes model for studies of the ocean on parallel computers. J. Geophys. Res. 102 (C3), 5753–5766.

Martin, A. P., Richards, K. J., Law, C. S., Liddicoat, M., 2001. Horizontal dispersion within an anticyclonic mesoscale eddy. Deep-Sea Res. II 48 (4–5), 739–755, the Biological Oceanography of the north-east Atlantic-the PRIME study.
URL `http://www.sciencedirect.com/science/article/B6VGC-41WJ%B12-5/2/1ac8a0644e4808644fd76081c644c27a`

McDonnell, A. M. P., Buesseler, K. O., 2010. Variability in the average sinking velocity of marine particles. Limnol. Oceanogr. 55 (5), 2085–2096.

MITgcm Group, 2012. MITgcm User Manual. Online documentation, MIT/EAPS, Cambridge, MA 02139, USA, `http://mitgcm.org/public/r2_manual/latest/online_documents`.

Parekh, P., Follows, M. J., Boyle, E., 2004. Modeling the global ocean iron cycle. Global Biogeochem. Cycles 18 (1), GB1002, doi:10.1029/2003GB002061.

Peloquin, J. A., Smith Jr., W. O., 2006. The role of phytoplankton size on photochemical recovery during the Southern Ocean iron experiment. J. of Phycology 42 (5), 1016–1027.

Sarmiento, J. L., Monfray, P., Maier-Reimer, E., Aumont, O., Murnane, R., Orr, J. C., 2000. Sea-air CO2 fluxes and carbon transport: a comparison of three ocean general circulation models. Global Biogeochem. Cycles 14 (4), 1267–1281.

Schartau, M., Engel, A., Schröter, J., Thoms, S., Völker, C., Wolf-Gladrow, D., 2007. Modelling carbon overconsumption and the formation of extracellular particulate organic carbon. Biogeosciences 4 (4), 433–454.
URL `http://www.biogeosciences.net/4/433/2007/`

Schartau, M., Oschlies, A., 2003. Simultaneous data-based optimization of a 1D-ecosystem model at three locations in the North Atlantic Ocean: Part I – Method and parameter estimates. J. Mar. Res. 61 (6), 765–793.

Schröter, J., Seiler, U., Wenzel, M., 1993. Variational assimilation of GEOSAT data into a eddy-resolving model of the Gulf Stream extension area. J. Phys. Oceanogr. 23 (5), 925–953.

Seiler, U., 1993. Estimation of open boundary conditions with the adjoint method. J. Geophys. Res. 98 (C12), 22855–22870.

Smetacek, V., Bathmann, U., Helmke, E. (Eds.), 2005. The expeditions ANTARKTIS XXI/3-4-5 of the Research Vessel "Polarstern" in 2004. Vol. 500 of Reports on Polar and Marine Research. Alfred-Wegener-Institut für Polar- und Meeresforschung, Bremerhaven, Germany.

Smetacek, V., Klaas, C., Strass, V. H., Assmy, P., Montresor, M., Cisewski, B., Savoye, N., Webb, A., d'Ovidio, F., Arrieta, J. M., Bathmann, U., Bellerby, R., Berg, G. M., Croot, P., Gonzalez, S., Henjes, J., Herndl, G. J., Hoffmann, L. J., Leach, H., Losch, M., Mills, M. M., Neill, C., Peeken, I., Röttgers, R., Sachs, O., Sauter, E., Schmidt, M. M., Schwarz, J., Terbrüggen, A., Wolf-Gladrow., D., 2012. Deep carbon export from a Southern Ocean iron-fertilized diatom bloom. Nature 487, 313–319. URL `http://www.nature.com/nature/journal/v487/n7407/full/na% ture11229.html`

Smith, S. L., Yamanaka, Y., 2007. Quantitative comparison of photoacclimation models for marine phytoplankton. Ecol. Model. 201 (3–4), 547–552. URL `http://www.sciencedirect.com/science/article/B6VBS-4M6S% G9C-3/2/71cb84e8e988e0837bb0a31c27615fa9`

Stammer, D., 2005. Adjusting internal model errors through ocean state estimation. J. Phys. Oceanogr. 35 (6), 1143–1153.

Stammer, D., Wunsch, C., Giering, R., Eckert, C., Heimbach, P., Marotzke, J., Adcroft, A., Hill, C., Marshall, J., 2003. Volume, heat and freshwater transports of the global ocean circulation 1992–1997, estimated from a general circulation model constrained by WOCE data. J. Geophys. Res. 108 (C1), 3007, doi:10.1029/2001JC001115.

Stammer, D., Wunsch, C., Giering, R., Eckert, C., Heimbach, P., Marotzke, J., Adcroft, A., Hill, C. N., Marshall, J., 2002. The global ocean circulation during 1992–1997, estimated from ocean observations and a general circulation model. J. Geophys. Res. 107 (C9), 3118, doi:10.1029/2001JC000888.

Stanton, T. P., Law, C. S., Watson, A. J., 1998. Physical evolution of the IronEx-I open ocean tracer patch. Deep-Sea Res. II 45 (6), 947–975.

URL `http://www.sciencedirect.com/science/article/B6VGC-3VFG%VHM-3/2/ea02a62a8cc2c77734fec59c6e3d0073`

Strass, V., Cisewski, B., Gonzalez, S., Leach, H., Loquay, K.-D., Prandke, H., Rohr, H., Thomas, M., 2005. The physical setting of the European Iron Fertilization Experiment "EIFEX" in the Southern Ocean. In: Smetacek et al. (2005), pp. 15–36.

Taylor, M. H., Losch, M., Bracher, A., 2013. On the drivers of phytoplankton blooms in the Antarctic seasonal ice zone: a modeling approach. J. Geophys. Res. 118 (1), 63–75.

Thacker, W. C., Long, R., 1988. Fitting dynamics to data. J. Geophys. Res. 93 (C2), 1227–1240.

Vogeler, A., Schröter, J., 1999. Fitting a regional ocean model with adjustable open boundaries to TOPEX/POSEIDON data. J. Geophys. Res. 104 (C9), 20789–20799.

Wessel, P., Smith, W. H. F., 1998. New, improved version of the Generic Mapping Tools released. Eos Trans. AGU 79 (579).

Wunsch, C., 2006. Discrete Inverse and State Estimation Problems. With Geophysical Applications. Cambridge University Press, Cambridge.

Zhang, K. Q., Marotzke, J., 1998. The importance of open-boundary estimation for an Indian Ocean GCM-data synthesis. J. Mar. Res. 57, 305–334.